

Surface Boundary Conditions During Long-Term Climate Change

NWMO-TR-2015-16

September 2015

Gordan Stuhne and W. Richard Peltier

University of Toronto, Department of Physics

nwmo

NUCLEAR WASTE
MANAGEMENT
ORGANIZATION

SOCIÉTÉ DE GESTION
DES DÉCHETS
NUCLÉAIRES



Nuclear Waste Management Organization
22 St. Clair Avenue East, 6th Floor
Toronto, Ontario
M4T 2S3
Canada

Tel: 416-934-9814
Web: www.nwmo.ca

Surface Boundary Conditions During Long-Term Climate Change

NWMO-TR-2015-16

September 2015

Gordan Stuhne and W. Richard Peltier
University of Toronto, Department of Physics

This report has been prepared under contract to NWMO. The report has been reviewed by NWMO, but the views and conclusions are those of the authors and do not necessarily represent those of the NWMO.

All copyright and intellectual property rights belong to NWMO.

Document History

Title:	Surface Boundary Conditions During Long-Term Climate Change		
Report Number:	NWMO-TR-2015-16		
Revision:	R000	Date:	September 2015
University of Toronto, Department of Physics			
Authored by:	Gordan Stuhne and W. Richard Peltier		
Verified by:	W. Richard Peltier		
Approved by:	W. Richard Peltier		
Nuclear Waste Management Organization			
Verified by:	Eric Sykes		
Reviewed by:	Eric Sykes		
Accepted by:	Mark Jensen		

ABSTRACT

Title: Surface Boundary Conditions During Long-Term Climate Change
Report No.: NWMO-TR-2015-16
Author(s): Gordan Stuhne and W. Richard Peltier
Company: University of Toronto
Date: September 2015

Abstract

The latest version of the University of Toronto Glacial Systems Model (UofTGSM) was employed in the development of data sets describing the evolution of surface boundary conditions above a potential spent fuel repository over the course of a 122.5 kyr cycle of glaciation. The new data sets build increased confidence upon the previous UofTGSM-generated data sets that Peltier (2006) supplied for this purpose. The components of the UofTGSM have been updated to a framework reflecting the current state-of-the-art, and a new strategy has been adopted to preserve consistency with observations independently of detailed assumptions about ice-sheet dynamics. A mass-balance adjustment is employed to nudge the ice-thickness solution towards the observationally well-validated ICE-6G_C reconstruction, and dynamical variability can be analyzed in the context of ensembles with different exponential relaxation time-scales. This approach is used to diagnose ice thickness, permafrost thickness, basal temperature, meltwater production, lake depth, and other two-dimensional, time-varying fields from a reference solution along with corresponding local error estimates. Beyond reflecting significant numerical advances that enabled the new UofTGSM to better represent basal processes, ice-shelves, temperate ice-water mixtures and other physics, the new results benefit from the many new measurements that constrained ICE-6G_C (and therefore, indirectly, the nudged paleoclimate simulations). Nudging offers a more practical approach to leading-order data assimilation and error estimation than Bayesian calibration, which was employed in Peltier (2006), and which will continue to be of use in more detailed explorations of observationally constrained model parameter spaces. Rather than consisting of discrete time-series at the sites of hypothetical spent-fuel repositories, the new dataset also includes time-varying two-dimensional geographic distributions covering all of Canada.

TABLE OF CONTENTS

	<u>Page</u>
ABSTRACT	iii
1. INTRODUCTION	1
2. METHODOLOGY AND DATA SETS.....	2
2.1 Nudging and Paleoclimate Mass Balances	2
2.2 Ice-sheet Dynamical Model	4
2.3 GIA-SLA Solution	5
2.4 Greenland and Antarctic Validation Studies	7
2.5 Canadian Ice Sheet Simulation Calibration	14
2.6 Canadian Reference Solution Fields and Variability	20
2.7 Lake Depth	24
3. DISCUSSION	29
4. SUMMARY AND CONCLUSIONS	37
REFERENCES	39
APPENDIX A: CD ARCHIVE OF TIME SERIES	43

LIST OF FIGURES

		<u>Page</u>
Figure 1:	Schematic layout of the geometry of sea level, grounded ice, grounding lines, and floating ice shelves.....	6
Figure 2:	RSL curves from the $\tau_f = 20$ yr (red), $\tau_f = 100$ yr (blue), and $\tau_f = 200$ yr (green) Greenland simulations compared to I6G (black) and overlaid on observational data at the 16 stations discussed in TP02.	8
Figure 3:	RSL curves from the $\tau_f = 20$ yr (red), $\tau_f = 100$ yr (blue), and $\tau_f = 200$ yr (green) Antarctic simulations compared to I6G (black) and overlaid on observational data at the 12 stations discussed in Argus et al. (2014).	9
Figure 4:	Scatter plot comparing simulated uplift rates from cases with $\tau_f = 20$ yr (orange triangles), $\tau_f = 100$ yr (cyan squares), and $\tau_f = 200$ yr (blue diamonds) with I6G (red circles) and with observations at the 42 stations depicted in Figure 5 (grey error bars spanning data variance).....	10
Figure 5:	Modern vertical displacement rates (in mm/s) computed for Antarctica by applying the full GIA-SLA theory to I6C (left) and to simulation results with $\tau_f = 20$ yr (middle). The right frame shows the difference between the two, and the locations of the 42 sites at which Argus et al. (2014) compared I6G to GPS observations.	11
Figure 6:	Modern vertical displacement rate misfits analogous to the right ($\tau_f = 20$ yr) frame in Figure 5 for $\tau_f = 100$ yr (left) and $\tau_f = 200$ yr (right) nudging time scales.	12
Figure 7:	Greenland (top row) and Antarctic (bottom row) mass balances from nudging term, ΔG , for relaxation to I6G with (a) $\tau_f = 20$ yr (left); (b) $\tau_f = 100$ yr (middle); and (c) $\tau_f = 200$ yr (right).	13
Figure 8:	RSL curves from the $\tau_f = 20$ yr (red), $\tau_f = 100$ yr (blue), $\tau_f = 200$ yr (green), and $\tau_f = 1000$ yr (orange) North American simulations compared to I6G (black) and overlaid on observational data at the 18 stations discussed in Peltier et al. (2015).	15
Figure 9:	Scatter plot comparing simulated uplift rates from cases with $\tau_f = 20$ yr (orange triangles), $\tau_f = 100$ yr (cyan squares), $\tau_f = 200$ yr (blue diamonds), and $\tau_f = 1000$ yr (green inverted triangles) with I6G (red circles) and with observations at representative stations.	16

Figure 10:	Modern vertical displacement rates (in mm/s) computed for Canada by applying the full GIA-SLA theory to I6C (left) and to simulation results with $\tau_f = 20$ yr (middle). The right frame shows the difference between the two, and the locations of the 51 sites at which I6G to GPS observations are compared.	17
Figure 11:	Modern vertical displacement rate misfits analogous to the right ($\tau_f = 20$ yr) frame in Figure 10 for $\tau_f = 100$ yr (left), $\tau_f = 200$ yr (middle), and $\tau_f = 200$ yr (right) nudging time scales.	18
Figure 12:	North American mass balances from the nudging term, ΔG in simulations with $\tau_f = 20$ yr (upper left), $\tau_f = 100$ yr (upper right), $\tau_f = 200$ yr (lower left), and $\tau_f = 1000$ yr (lower right).	19
Figure 13:	Reference solution ice thickness, I (left), and error, ΔI (right), at $t = 26$ kyr BP (LGM), 14.2 kry BP, 9 kry BP, and present.	21
Figure 14:	Permafrost thickness and corresponding error from the solution referenced in Figure 13.	22
Figure 15:	Basal temperature and corresponding error from the solution referenced in Figure 13.	23
Figure 16:	Basal meltwater production and corresponding error from the solution referenced in Figure 13.	25
Figure 17:	Basal velocity and corresponding error from the solution referenced in Figure 13.	26
Figure 18:	Vertical basal shear stress and corresponding error from the solution referenced in Figure 13.	27
Figure 19:	Lake depth and corresponding error from the solution referenced in Figure 13.	28
Figure 20:	Composite contour plots of grounded ice elevation, floating ice thickness, and lake depth at times considered in Peltier (2006).	30
Figure 21:	Continuation of Figure 20.	31
Figure 22:	Continuation of Figures 20 and 21.	32
Figure 23:	Time series of selected fields at the 4CS site, shown with error margins and compared with the nn2008 and nn2778 cases of Peltier (2006).	33

- Figure 24: Time series of selected fields at the 5CS site, shown with error margins and compared with the nn9921 and nn9930 cases of Peltier (2011). 34
- Figure 25: Time series of climatological temperature adjustment, $\Delta T(t)$, inferred from the Greenland GRIP ice core (black) and the Antarctic Vostok ice core (red). The SPECMAP time series of eustatic sea-level change is shown (in blue) along with a version corrected for ocean temperature (green) and an estimate based on eustatic sea-level equivalent I6G ice volume change (in violet). The y -scale for sea levels is shown on the right axis. 35

1. INTRODUCTION

In a technical report and accompanying data sets previously submitted to NWMO, Peltier (2006) discussed an ensemble of numerical simulations of the evolution of North American ice-sheets over the last glacial cycle (~ 100 kyr BP to present). The objective of these analyses was to provide a set of surface boundary conditions and corresponding error estimates for assessing the potential effects of future ice age glaciation on an underground Deep Geologic Repository. The simulations were carried out using an early version of the University of Toronto Glacial Systems Model (UofTGSM), and the particular parameter selections defining the ensemble derived from the application of a Bayesian calibration technique that tuned the model to observational constraints involving radiocarbon-dated evidence of past relative sea levels and ice margins, as well as modern measurements of surface gravity and of the vertical motion of the solid surface (Tarasov and Peltier, 1997, 1999, 2000, 2002, 2003, 2004) (hereafter TP_{xx}). Results from the entire ensemble were represented in terms of local time series of ice velocity, normal stress, basal temperature, basal meltwater production, and proglacial lake depth at the site of interest, and in terms of global time series of ice sheet volume and surface area. Selected solutions from the ensemble were also used to represent the site-specific depth-time distribution of temperature in a lithospheric layer (in order to assess permafrost depth), as well as the continental-scale distributions of ice-sheet surface elevations (for glaciated areas) and proglacial lakes (for unglaciated areas).

Ice-sheet models have become considerably more sophisticated than the original UofTGSM, and even the technology that is state-of-the-art as of the present day will likely evolve further with an attendant proliferation in the number of “tunable” parameters. The simulated physics of floating-ice shelves, grounding lines, and basal processes at the ice-sheet-solid surface interface are particularly sensitive to poorly constrained parameterizations, and our lack of knowledge about paleoclimatological conditions at the ice surface (specifically, temperature, precipitation, ablation, etc.) also opens the door to the virtually unlimited expansion of model parameter spaces. This Report describes the production of new boundary condition (BC) datasets in a framework that addresses the aforementioned issues while incorporating the latest observational data and updating the UofTGSM framework based upon the current state-of-the-art in physical and computational science. Beyond being derived from a more sophisticated ice-sheet dynamical approximation and validated with respect to a more complete array of observational constraints, the new results benefit from a fundamentally enhanced scientific approach that better captures the true empirical uncertainties in the simulation of paleoclimate scenarios. Regardless of their level of sophistication, ice-sheet dynamical models fundamentally serve to determine ice-sheet thickness history, $l(\Omega, t)$, through the universal two-dimensional ice conservation law:

$$\frac{\partial l}{\partial t} + \nabla_h \cdot \mathbf{Q}(\Omega, t; \Pi_1, \dots, \Pi_n) = G(\Omega, t; \Pi_1, \dots, \Pi_n) \quad (1)$$

in which $\mathbf{Q}(\Omega, t; \Pi_1, \dots, \Pi_n)$ and $G(\Omega, t; \Pi_1, \dots, \Pi_n)$ denote the horizontal ice flux and source terms of a generic ice-sheet model with dynamical parameters Π_1, \dots, Π_n . The Bayesian techniques of TP_{xx} aimed to select Π_i for consistency with observations, but their practical success was limited by the *a priori* assumption of restrictive mathematical forms for ice flux, \mathbf{Q} , and net mass balance, G .

Rather than relying entirely upon a standard approach that determines paleoclimate BCs by adjusting modern distributions of temperature and mass balance based upon ice-core records of ancient $\delta^{18}\text{O}$ distributions (Ritz et al., 1996), the new approach adjusts G in such a way as to “nudge” ice thickness history, $I(\Omega, t)$, towards the observationally pre-validated ICE-6G_C reconstruction (hereafter I6G) (Argus et al., 2014; Peltier et al., 2015). Along with the VM5a reconstruction of radially varying mantle viscosity, I6G derives from a pure glacial isostatic adjustment (GIA)-based “inverse method” that fits $I(\Omega, t)$ independently of ice-sheet model assumptions (Peltier, 1974, 1976a,b; Peltier and Andrews, 1976; Farrell and Clark, 1976; Clark et al., 1978; Peltier et al., 1978; Peltier, 1998, 2007; Peltier et al., 2015). The details of a new approach that reconciles GIA-based methods with ice-sheet dynamical modelling are described in Stuhne and Peltier (2015) (SP), which also describes its validation with respect to the I6G reconstructions of Greenland and Antarctica. Some of the key points from SP will be summarized in the following Section, which also describes the setup and information content of the new ensemble of Canadian glacial simulations. The Discussion considers how the dataset meets the scientific and technical requirements of NWMO along with possible directions for further work. A summary of what has been achieved will appear in the Summary and Conclusions.

2. METHODOLOGY AND DATA SETS

2.1 Nudging and Paleoclimate Mass Balances

The nudging procedure can be framed independently of the details of the ice-sheet dynamics by rewriting the ice conservation equation (1) as follows: i.e.,

$$\begin{aligned} \frac{\partial I}{\partial t} + \nabla_h \cdot \mathbf{Q}(\Omega, t; \Pi_1, \dots, \Pi_n) &= G(\Omega, t; \Pi_1, \dots, \Pi_n) + \Delta G(\Omega, t; \tau_f), \\ \Delta G(\Omega, t; \tau_f) &= -\frac{[I(\Omega, t) - I_{i6g}(\Omega, t)]}{\tau_f}, \end{aligned} \quad (2)$$

in which the mass balance adjustment, ΔG , exponentially relaxes the evolving ice thickness, I , towards the I6G solution, I_{i6g} , at the time scale τ_f . This procedure, which borrows from standard techniques of multi-scale atmosphere-ocean modelling (e.g., Salameh et al., 2010), expands the discrete parameter space of the original model with the single parameter τ_f . Not being fully determined by the observational data that it is fit to and remaining subject to potential error and

non-uniqueness, the I_{i6g} reconstruction also brings with it an implicit expansion of the continuous parameter space of the original model. In this regard, however, it is much less open-ended than the assumptions that ice-sheet dynamical models must make about ice-atmosphere, ice-surface, and ice-ocean interactions in order to constrain the surface and basal components (G_s and G_b , respectively) of net mass balance,

$$G = G_s + G_b,$$

which is further complicated by implicit contributions arising from numerical constraints that enforce positive ice thickness and implement kinematic calving boundary conditions over paleoclimate time-scales (see SP for more mathematical details). Surface mass balance, G_s , is typically adjusted in tandem with other paleoclimate BCs based on time series, $\delta^{18}\text{O}(t)$, of ^{18}O concentration inferred from ice-core measurements. Surface temperature, $T_{\text{surf}}(\Omega, t)$, and precipitation, $P_{\text{surf}}(\Omega, t)$, are routinely assumed to deviate from modern ($t = 0$) climatology by the following relations:

$$\begin{aligned} T_{\text{surf}}(\Omega, t) &= T_{\text{surf}}(\Omega, 0) + \Delta T(t) \\ P_{\text{surf}}(\Omega, t) &= P_{\text{surf}}(\Omega, 0) \times \exp[\eta \Delta T(t)], \\ \Delta T(\Omega, t) &= \alpha_c^{-1} [\delta^{18}\text{O}(t) - \delta^{18}\text{O}(0)] \end{aligned} \quad (3)$$

in which α_c is an empirical constant relating globally constant temperature deviation, $\Delta T(t)$, to the $\delta^{18}\text{O}$ time-series and η is another empirical constant relating it to local precipitation change (Ritz et al., 1996). Even granting that Eq. (3) allows for the inference of past climate change “close to” the extraction sites of the Greenland Ice Core Project (GRIP) ice core on Greenland (Johnsen et al., 1997) and the Vostok ice core on Antarctica (Petit et al., 2001), it is an oversimplification to geographically extrapolate constant variations over the much larger scales of ice-sheet simulations. The actual estimate of G_s becomes even more tenuous when the estimated paleoclimatological temperature and precipitation are passed through a positive degree day (PDD) scheme that statistically models the balance between accumulation and ablation. Concerning the *basal* component, G_b , of the mass balance G , still greater dimensions of uncertainty open up with the need to estimate melting and freezing at the bases of floating ice shelves and at the interfaces between grounded ice sheets and the solid surface (e.g., Pollard and DeConto, 2009; Joughin et al., 2014). Considering that the source term in Eq. (2) is underconstrained from the outset, it is more fruitful to think of “nudged” rational dynamics as a mechanism for “smoothing,” or “correcting,” the I_{i6g} reconstruction.

Since the Canadian ice-sheet was far removed from the sites where modern Greenland and Antarctic ice cores were recovered, a more natural alternative to Eqs. (3) entails interpolating surface temperature and precipitation between modern and last glacial maximum (LGM, $t = t_{\text{LGM}} \approx$

26ka BP) solutions from a coupled climate model (Marshall et al., 2000). Peltier (2006) based the time-series of interpolation coefficients upon the Greenland ^{18}O record, but it is most natural in “nudged” simulations to infer climate states based upon the I6G-reconstructed North American ice-sheet volume time series, $V(t)$: i.e.,

$$\begin{aligned} T_{\text{surf}}(\Omega, t) &= \phi(t) T_{\text{surf}}(\Omega, 0) + [1 - \phi(t)] T_{\text{surf}}(\Omega, t_{\text{LGM}}) \\ P_{\text{surf}}(\Omega, t) &= \phi(t) P_{\text{surf}}(\Omega, 0) + [1 - \phi(t)] P_{\text{surf}}(\Omega, t_{\text{LGM}}) \\ \phi(t) &= \frac{V(t) - V(t_{\text{LGM}})}{V(0) - V(t_{\text{LGM}})}, \end{aligned} \quad (4)$$

in which $\phi(t)$ is the interpolation coefficient, $V(0)$ is the modern volume (≈ 0) and $V(t_{\text{LGM}})$ is the LGM volume at $t_{\text{LGM}} \approx -26$ ka BP. The details of “fiat” assumptions along the lines of Eqs. (3) and (4) are not particularly significant when combined with “nudging,” which would relax ice thickness towards the GIA-based reconstruction for any reasonable choice of paleoclimate BCs. The detailed tuning of mass balances inheres mostly in the prior reconstruction of I_{i6g} , but this study will defer to past work in dynamical ice-sheet modelling by prescribing the “base” mass balance, G , consistently with Eqs. (3) for the Greenland and Antarctic validation studies of SP, and consistently with Eqs. (4) for the Canadian glacial simulations described herein.

2.2 Ice-sheet Dynamical Model

Three-dimensional thermomechanical ice models determine \mathbf{Q} in Eqs. (2) as a vertical integral of velocity over the ice column: i.e.,

$$\mathbf{Q}(\Omega, t) = \int_{z=B_i}^H \mathbf{u}(\Omega, z, t) dz, \quad (5)$$

in which $B_i(\Omega, t)$ and $H(\Omega, t) = B_i(\Omega, t) + I(\Omega, t)$ are the respective displacements of the ice base and surface with respect to local sea level, and in which $\mathbf{u}(\Omega, z, t)$ is a three dimensional ice velocity vector that can be projected onto an horizontal polar stereographic coordinate system addressed by the following notations: i.e.,

$$\begin{aligned} \mathbf{u}(\mathbf{x}, t) &\equiv \begin{bmatrix} u \\ v \\ w \end{bmatrix} (x, y, z, t) = \begin{bmatrix} u_1 \\ u_2 \\ u_3 \end{bmatrix} (x_1, x_2, x_3, t) \\ &= u\hat{\mathbf{x}} + v\hat{\mathbf{y}} + w\hat{\mathbf{z}} = u_1\hat{\mathbf{x}}_1 + u_2\hat{\mathbf{x}}_2 + u_3\hat{\mathbf{x}}_3. \end{aligned} \quad (6)$$

For polythermal (“cold”) ice, the most physically complete determination of velocity is achieved through the Full Stokes (FS) model (e.g., Pattyn et al., 2008) that represents \mathbf{u} in tandem with the

scalar pressure and temperature fields ($p(x, y, z, t)$ and $T(x, y, z, t)$, respectively) as the solution of the following system of partial differential equations: i.e.,

$$\begin{aligned}
\nabla \cdot \mathbf{u} &= 0 & \nabla \cdot \boldsymbol{\sigma}_i &= \frac{\partial}{\partial x_i} (p + \rho_i g x_3) \\
\boldsymbol{\sigma}_i &\equiv \nu \boldsymbol{\varepsilon}_i & \boldsymbol{\varepsilon}_i &\equiv \nabla u_i + \frac{\partial \mathbf{u}}{\partial x_i} \\
\nu &= \frac{1}{2} \epsilon [\epsilon A(T, p)]^{-\frac{1}{n}} & \epsilon &\equiv \sqrt{\sum_{i=1}^3 \boldsymbol{\varepsilon}_i \cdot \boldsymbol{\varepsilon}_i} \\
\frac{\partial}{\partial t} [\rho_i c_i(T) T] + \nabla \cdot [\rho_i c_i(T) T \mathbf{u} - \kappa \nabla T] &= 4\nu \epsilon^2
\end{aligned} \tag{7}$$

in which g is acceleration due to gravity, ρ_i is the density of ice, $\boldsymbol{\varepsilon}_i$ and $\boldsymbol{\sigma}_i$ are the respective i^{th} rows of the strain rate and deviatoric stress tensors (for $i = 1, 2$, or 3), $A(T, p)$ is a phenomenological “ice hardness” function that introduces thermodynamic effects into the Glen flow law for determining plastic viscosity, ν , in terms of strain amplitude, ϵ , and an exponent, n , and κ and $c_i(T)$ are the thermal diffusivity and temperature-dependent specific heat capacity of ice, respectively. By using enthalpy instead of temperature in a more sophisticated analogue of the system (7), one can achieve an even more complete FS model in which ice may exhibit not only polythermal regions, but also temperate regions where it is at its pressure-dependent melting point, and where it coexists with meltwater.

To integrate practical ice-sheet dynamical simulations over large space and time scales, the FS equations (7) must in practice be completed with suitable BCs and subjected to various levels of physical approximation before the resulting simplified equation systems are discretized and numerically solved. Physical and numerical approximations raise complex issues which were discussed at length in SP. The new UofTGSM is best regarded not as a single model with a fixed parameter space, but as a framework for bringing a variety of approximations and numerical techniques to bear on a phenomenon of interest. For purposes of the validation studies of Greenland and Antarctica (SP) and the present calculation of Canadian surface BCs under glacial conditions, SP used the coupled shallow-ice-shelfy stream approximation (SIA-SSA) implemented in the highly parallelized, structured-grid-based dynamical core of the parallel ice sheet model (PISM) (Winkelmann et al., 2011).

2.3 GIA-SLA Solution

In the definition (5) of the horizontal ice flux, the displacement of the ice base, $B_i(\Omega, t)$, depends upon whether the ice column is grounded or floating, and Figure 1 clarifies the geometry of this boundary in relation to the solid surface, $B(\Omega, t)$, the ice surface $H(\Omega, t)$, and the geoid. $B_i(\Omega, t)$

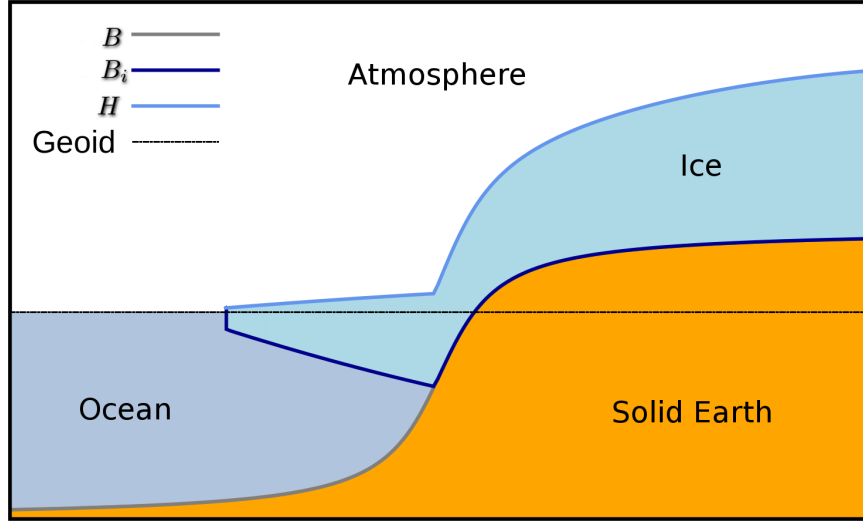


Figure 1: Schematic layout of the geometry of sea level, grounded ice, grounding lines, and floating ice shelves.

can be determined as follows: i.e.,

$$B_i(\Omega, t) = \begin{cases} -\frac{\rho_i l(\Omega, t)}{\rho_w} & \text{for floating ice where } C(\Omega, t) = 1 \\ B(\Omega, t) & \text{for grounded ice where } C(\Omega, t) = 0, \end{cases} \quad (8)$$

in which ρ_w is the density of water, $B(\Omega, t)$ is the displacement of the solid surface with respect to the contemporary geoid (i.e., absolute sea level at time t), and $C(\Omega, t)$ is a binary indicator function that masks out land and grounded ice based on Archimedes principle by vanishing where

$$B(\Omega, t) + \frac{\rho_i l(\Omega, t)}{\rho_w} \geq 0,$$

and taking the value of unity elsewhere. Along with other generic fields, $\Upsilon(\Omega, t)$, associated with the GIA-SLA problem, $B(\Omega, t)$ can be computed by integral convolution with the total water-ice mass load, $L(\Omega, t)$, and the corresponding rotational load, $T(\Omega, t)$: i.e.,

$$\Upsilon(\Omega, t) = \int_{-\infty}^t \int \int_{\Omega} \left[L(\Omega', t') \Gamma^{\Upsilon, L}(\Omega, \Omega', t - t') + T(\Omega', t') \Gamma^{\Upsilon, T}(\Omega, \Omega', t - t') \right] d\Omega' dt', \quad (9)$$

in which the viscoelastic Green's functions, $\Gamma^{\Upsilon, L}(\Omega, \Omega', t - t')$ and $\Gamma^{\Upsilon, T}(\Omega, \Omega', t - t')$ are determined by the assumed radial distribution of mantle viscosity. The load terms in Eqs. (9) are determined by the following relations: i.e.,

$$L(\Omega, t) = \rho_i l(\Omega, t) + \rho_w S(\Omega, t)$$

$$T(\Omega, t) = \Omega_0 a^2 \left\{ \frac{\omega_3(t)}{3} [2Y_{00}(\Omega) - Y_{20}(\Omega)] + \sqrt{\frac{2}{15}} [\omega_1(t) - i\omega_2(t)] [Y_{21}(\Omega) - iY_{2-1}(\Omega)] \right\}, \quad (10)$$

in which $S(\Omega, t)$ is the relative sea level (RSL) determining the surface load of ocean and floating ice where $C = 1$ while vanishing elsewhere, a is the mean radius of the Earth, $Y_{lm}(\Omega)$ are the spherical harmonics of degree and order (l, m) , and

$$(\omega_1(t), \omega_2(t), \omega_3(t)) \approx (0, 0, \Omega_0)$$

is the time-varying pseudovector that represents variations in Earth's rotational state. For ice-thickness history, $I(\Omega, t)$, obtained either from direct construction (e.g., I_{i6g} for I6G) or from the solution of suitably approximated Eqs. (2) and (7), $S(\Omega, t)$ can be obtained through the iterative numerical solution of the gravitationally self-consistent SLE: i.e.,

$$S(\Omega, t) = C(\Omega, t) \left[\int_{-\infty}^t \int dt' \int_{\Omega} d\Omega' \left\{ L(\Omega', t') \Gamma^{S,L}(\Omega, \Omega', t - t') \right. \right. \\ \left. \left. + T(\Omega', t') \Gamma^{S,T}(\Omega, \Omega', t - t') \right\} + \frac{\Delta\Phi(t)}{g} \right], \quad (11)$$

in which $\Delta\Phi(t)$ follows the time-variation of the world ocean's gravitational equipotential. $\Delta\Phi(t)$ and $\omega_i(t)$ are determined through the respective enforcement of global mass and angular momentum constraints in the solution of Eq. (11) (Wu and Peltier, 1984; Peltier and Luthcke, 2009; Peltier et al., 2012).

For a given hypothesis about ice thickness, empirical validation is achieved by solving (11), comparing local observations of RSL with $S(\Omega, t)$, and comparing local GPS observations of vertical uplift rate with $\partial B/\partial t(\Omega, t)$ (computed from the numerical differentiation of Eq. (9) for $\Upsilon = B$). The time variation of $B(\Omega, t)$ also couples to dynamical simulations of $I(\Omega, t)$ through Eq. (5) and other ice-sheet model BCs, and a rigorous and fully coupled methodology would go even further by adjusting the local flotation criterion (8) to take into account space- and time-variations of gravitationally self-consistent RSL, $S(\Omega, t)$. For computational tractability in dynamical simulations, the computation of $B(\Omega, t)$ is implied by the assumption that $S = S_{i6g}$ and $T = T_{i6g}$ in Eq. (9). This permits only $I(\Omega)$ to dynamically influence bottom topography. In the flotation criterion (8), sea-level variation is everywhere associated with the eustatic component of I6G.

2.4 Greenland and Antarctic Validation Studies

To build confidence in the results produced by the methodology, and establish a starting point for its application to other continental ice-sheets, SP analyzed how ice-dynamical "smoothing" of the I6G (VM5a) representations of the Greenland and Antarctic ice-sheets affected the quality of agreement between observations and model predictions at different nudging time scales, τ_f . Greenland and Antarctica were selected as validation cases because their still-existing ice sheets have to some extent enabled paleoclimate models to be constrained with ice core data, modern

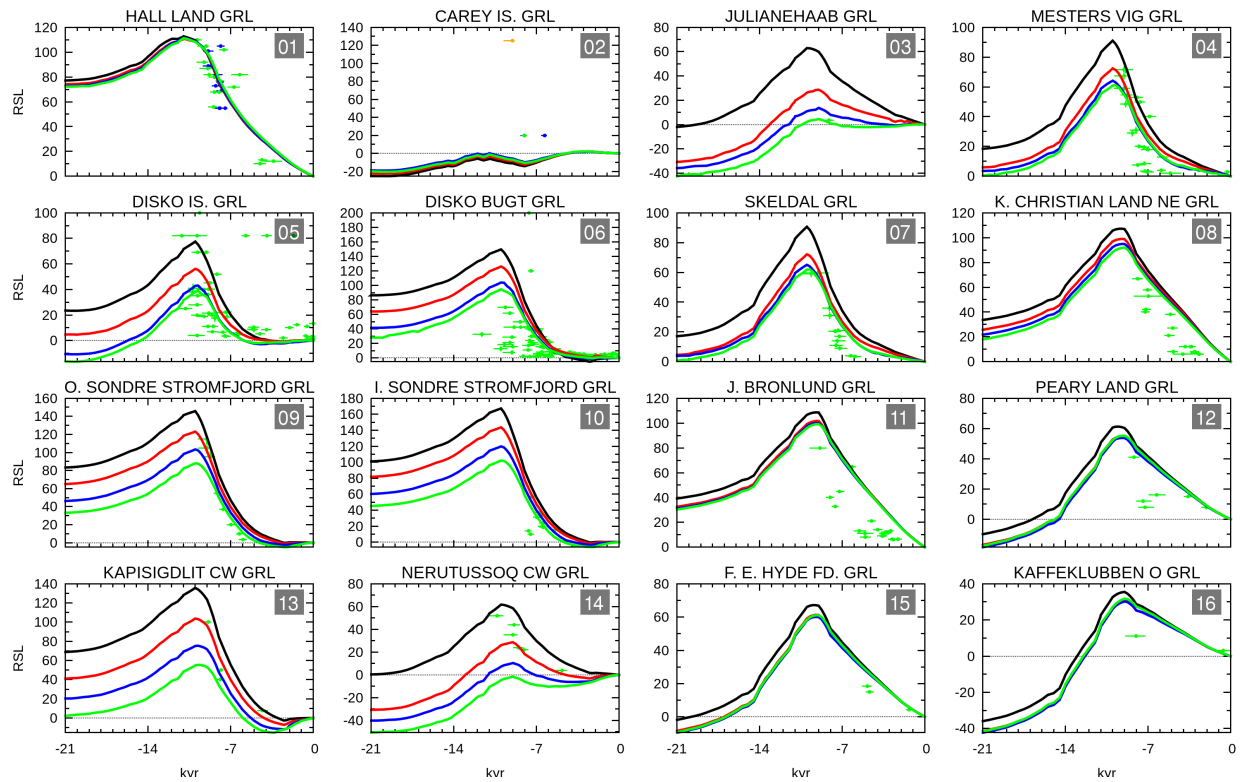


Figure 2: RSL curves from the $\tau_f = 20$ yr (red), $\tau_f = 100$ yr (blue), and $\tau_f = 200$ yr (green) Greenland simulations compared to I6G (black) and overlaid on observational data at the 16 stations discussed in TP02.

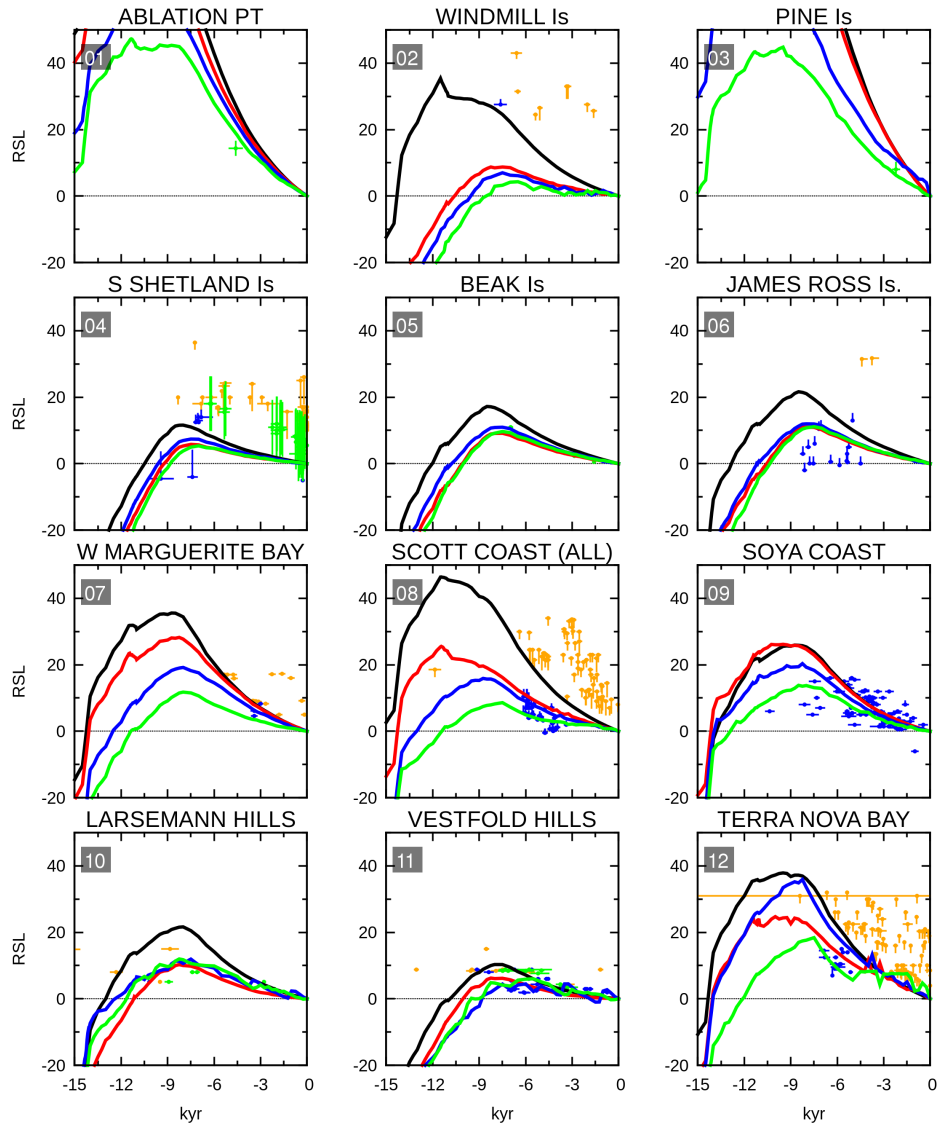


Figure 3: RSL curves from the $\tau_f = 20$ yr (red), $\tau_f = 100$ yr (blue), and $\tau_f = 200$ yr (green) Antarctic simulations compared to I6G (black) and overlaid on observational data at the 12 stations discussed in Argus et al. (2014).

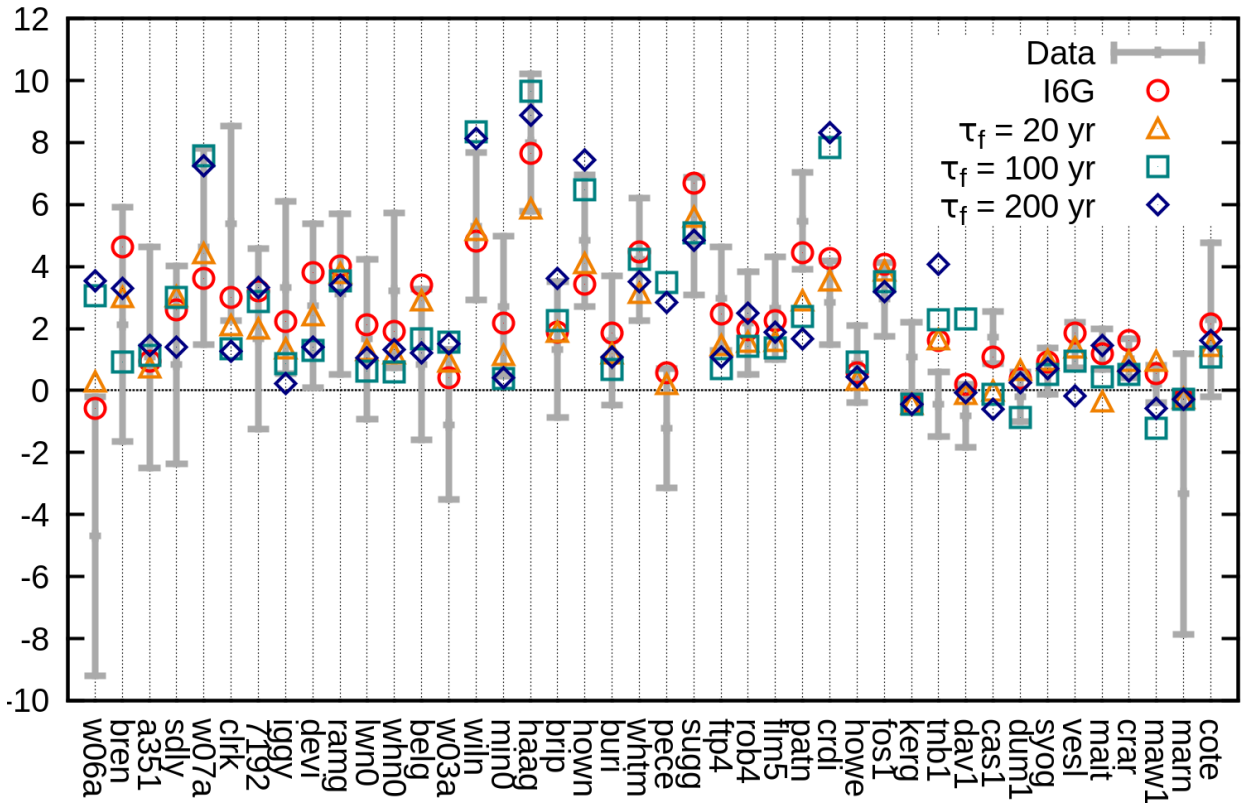


Figure 4: Scatter plot comparing simulated uplift rates from cases with $\tau_f = 20$ yr (orange triangles), $\tau_f = 100$ yr (cyan squares), and $\tau_f = 200$ yr (blue diamonds) with I6G (red circles) and with observations at the 42 stations depicted in Figure 5 (grey error bars spanning data variance).

glaciological measurements, and so on. The SeaRISE modelling initiative has established a corpus of relatively standardized modelling protocols and parameters for studying the past and future dynamics of these modern ice-sheets (Bindschadler et al., 2013; Nowicki et al., 2013a,b), and our approach enables us to extend the same “typical” parameter regime to all ice-sheets instead of attempting, generally with only partial success, to achieve observational fits and error estimates through the case-specific local adjustment of hundreds of parameters. The local dependence of solutions upon the nudging parameter, τ_f , provides for quantitative, intuitive, and systematic estimates of the degree to which ice-sheet dynamics may induce variations about the observationally validated I6G reconstruction. SP compared “envelopes” of $S(\Omega, t)$ and $\partial B/\partial t(\Omega, 0)$ predictions from simulations with different τ_f with the error bars and scatter in RSL and GPS observations of Greenland and Antarctica. The results of these analyzes are briefly summarized below.

Figures 2 and 3 compare RSL observations with model predictions for Greenland and Antarctica, respectively. Results are shown from 16 Greenland sites and 12 Antarctic sites where the

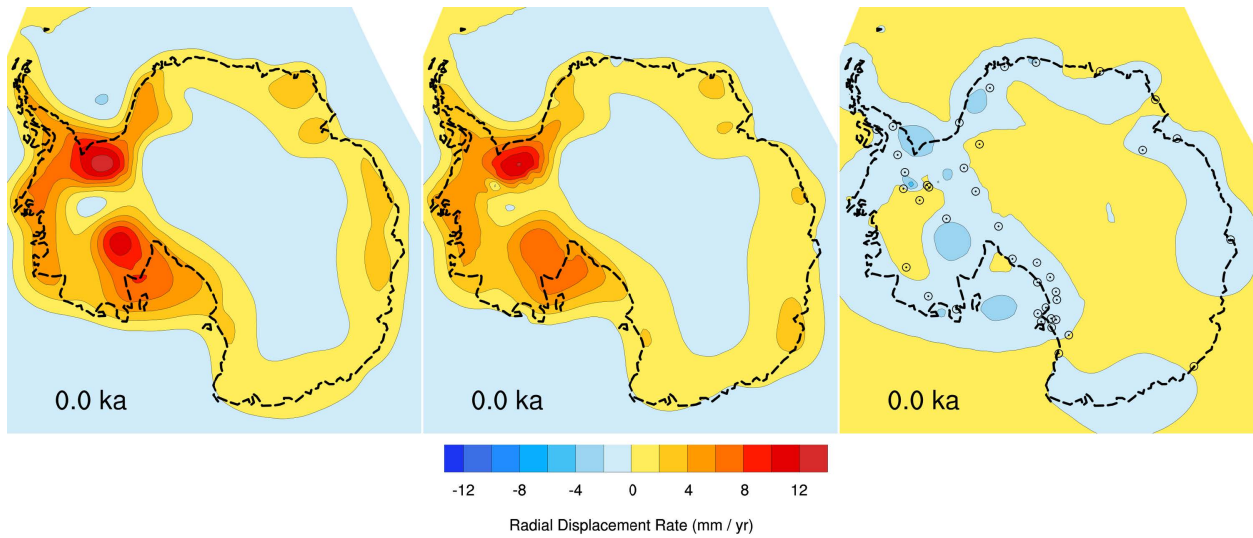


Figure 5: Modern vertical displacement rates (in mm/s) computed for Antarctica by applying the full GIA-SLA theory to I6C (left) and to simulation results with $\tau_f = 20$ yr (middle). The right frame shows the difference between the two, and the locations of the 42 sites at which Argus et al. (2014) compared I6G to GPS observations.

initial fits to the GIA-based reconstruction were considered in the respective studies of Tarasov and Peltier (2002) and Argus et al. (2014). In addition to reproducing the results from I6G (the black curves), the Figures show results from nudged simulations with $\tau_f = 20$ yr (the red curves), $\tau_f = 100$ yr (the blue curves), and $\tau_f = 200$ yr (the green curves). As should be expected on *a priori* grounds, curves almost always converge towards the I6G reference solution as τ_f decreases, while the ranges of RSL swept by the selected range of τ_f values reasonably bracket the variability suggested by observational error bars and scatter. The predicted extents of dynamical variability are consistent with the evidence of Figures 2 and 3, which suggest that the Greenland observations exhibit considerably less variability than their Antarctic counterparts. In the original fitting of the I6G reconstruction of Antarctic ice-thickness history to observations, high-quality GPS measurements of vertical surface motion at 42 key sites played a more significant role than the lower-quality RSL proxy measurements appearing in Figure 2. Figure 4 lists the GPS sites by their original database keys and compares observations of vertical motion (in mm/yr, and bracketted by grey error bars) with scatter plots of predictions from I6G and from the three nudged simulations. Nudged ice-sheet dynamics once again converge towards the original reconstruction results as τ_f decreases, and the range of vertical uplift rates swept by $\tau_f = 200$ yr, 100 yr, and 20 yr values once again reasonably predict the inherent uncertainty in the data.

To get a better picture of the geographical distribution of dynamical variability, one can consider Figures 5 and 6, which show 2-D contour plots comparing vertical motion predictions from

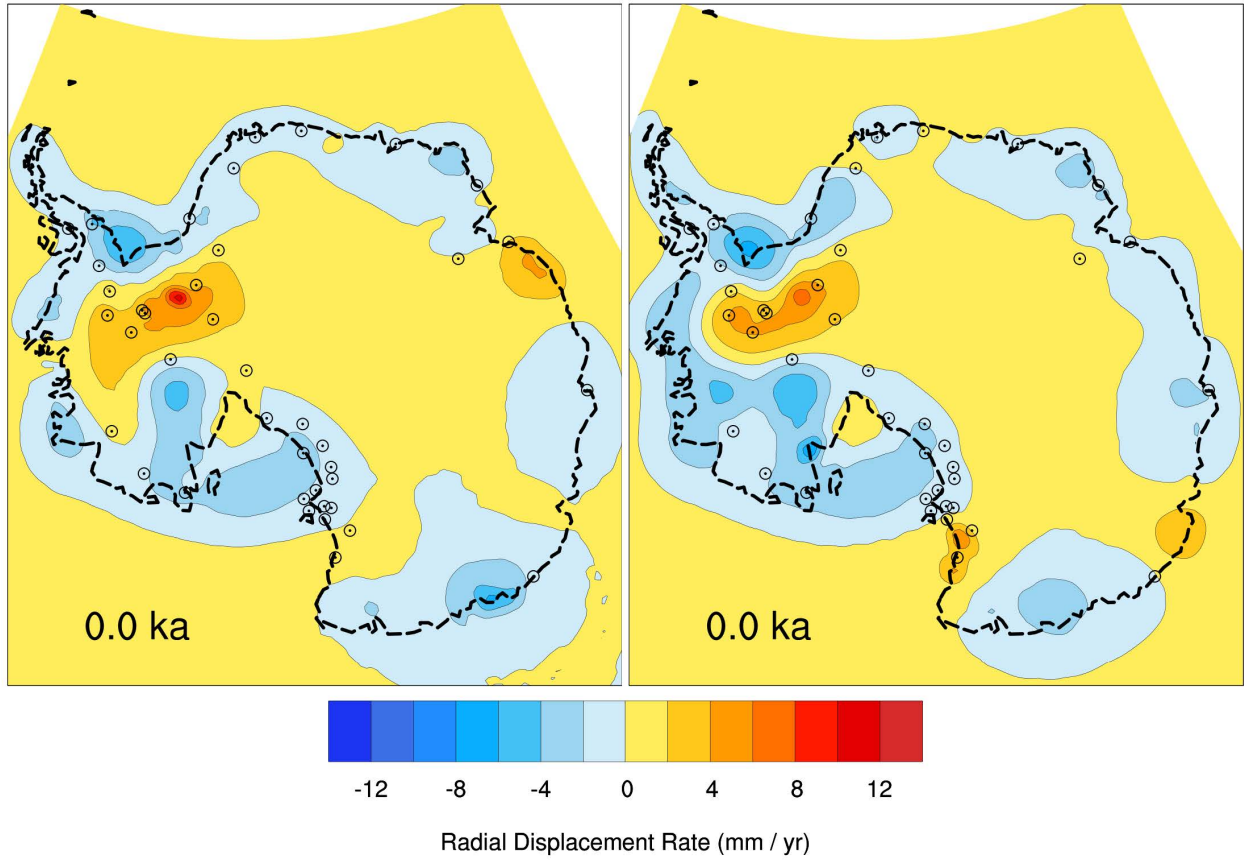


Figure 6: Modern vertical displacement rate misfits analogous to the right ($\tau_f = 20$ yr) frame in Figure 5 for $\tau_f = 100$ yr (left) and $\tau_f = 200$ yr (right) nudging time scales.

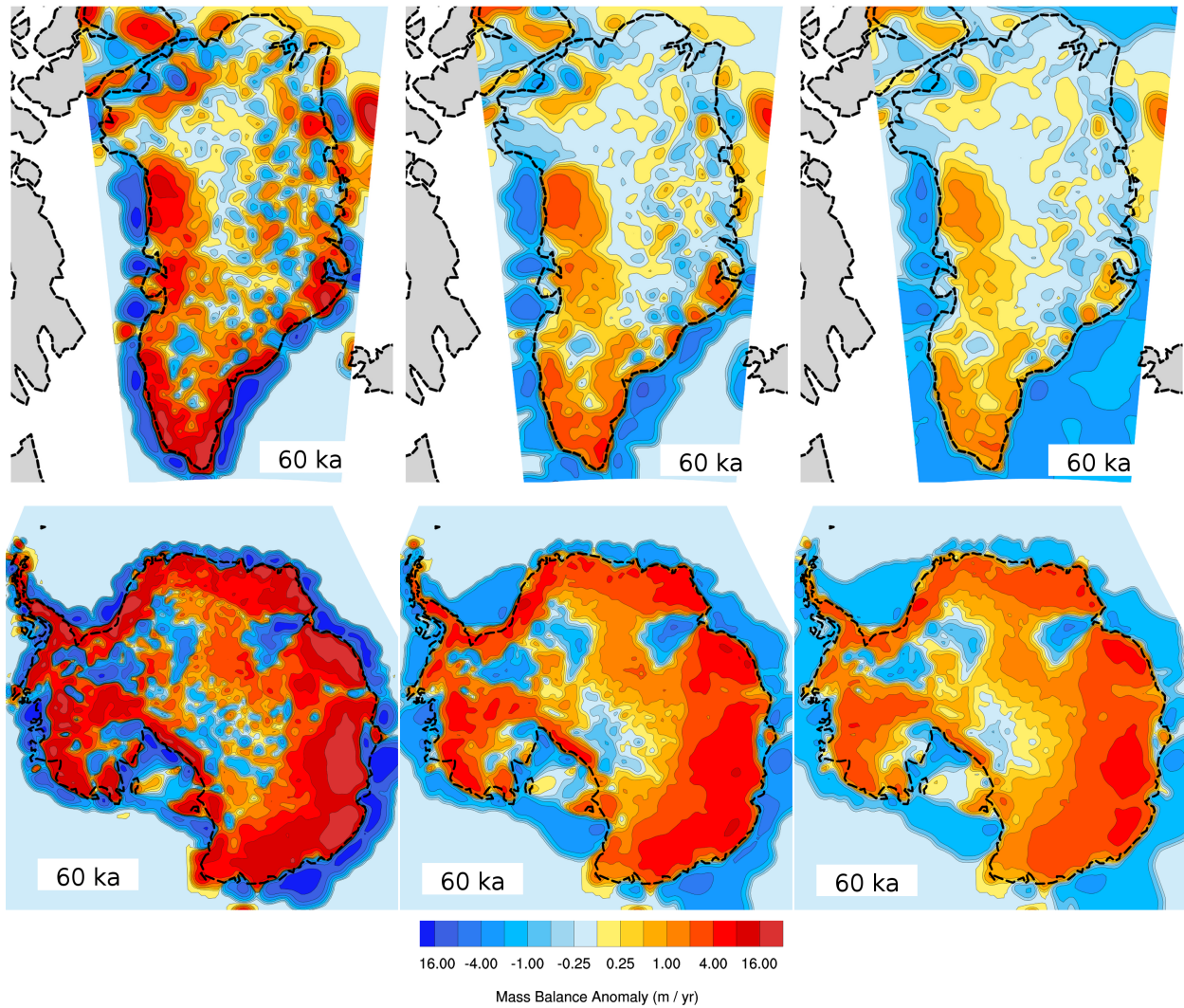


Figure 7: Greenland (top row) and Antarctic (bottom row) mass balances from nudging term, ΔG , for relaxation to 16G with (a) $\tau_f = 20$ yr (left); (b) $\tau_f = 100$ yr (middle); and (c) $\tau_f = 200$ yr (right).

I6G and the nudged simulations. Figure 5 compares the I6G prediction (the left frame) with the $\tau_f = 20$ yr prediction (the middle frame) and plots the difference between the two in the right frame along with the site labels corresponding to GPS observations. As shown in Figure 6, the deviations of nudged simulations from I6G grow to more significant amplitude as weaker nudging (i.e., increasing τ_f) allows for more dynamical variability. While achieving the best fit to I6G, the smallest ($\tau_f = 20$ yr) value also carries a “cost” in the sense that it implies the largest nudging mass balance adjustment, ΔG . Figure 7 depicts contour plots of ΔG at a representative time ($t = 60\text{kyr BP}$) from the Greenland and Antarctic cases and the three values of τ_f . In considering a range of τ_f bracketing the variability in the data that was used to fit the I6G reconstruction, one must also consider whether the implied distribution of ΔG is actually explainable in terms of ice-sheet dynamics, and in terms of our lack of knowledge thereof. Nudging mass balance adjustments of $\mathcal{O}(1 \text{ m/yr})$ and smaller (where \mathcal{O} denotes order of magnitude) are generally straightforward to explain in terms of uncertainty about surface precipitation and ablation under paleoclimate conditions. Figure 7 shows significant regions of both Greenland and Antarctica where the amplitude of ΔG exceeds this threshold by a considerable amount, but it is crucial to note that these are concentrated near coastlines, ice-sheet margins, and potential ice streams. These critical regions are subject to “catastrophic” mass transfers, whose representation in ice-sheet dynamical models is very crude. The validation experiments therefore indicate the consistency of the I6G reconstruction and of the methodology that has been applied to extract higher-order ice-dynamical information from it.

2.5 Canadian Ice Sheet Simulation Calibration

The principles that were applied in the Greenland and Antarctic validation studies can be transferred to the simulation of Canadian ice-sheet evolution. To emphasize presumed universality in large-scale ice dynamics, the SeaRISE parameter regime is used for all cases in a strategy that allows for consistent and easily intercomparable analyzes of geographically separated regional paleoclimate scenarios. Representing the analogue of the respective Figures 2 and 3 for Greenland and Antarctica, Figure 8 compares simulation RSL predictions to I6G at 18 North American sites that were referenced in the discussion of Peltier et al. (2015). Considering only the $\tau_f = 20$ yr, $\tau_f = 100$ yr, and $\tau_f = 200$ yr nudging time scales from the validation studies, one sees the dynamical predictions agreeing closely with I6G - so closely, in fact, as to make the swept RSL ranges considerably narrower than the error bars and scatter in the observational data. To better represent the observational variability with the ice-sheet dynamical model, the ensemble of simulations was expanded to include an even more weakly nudged simulation with $\tau_f = 1000$ yr. In the comparison of model-predicted $\partial B/\partial t(0)$ with modern GPS measurements at 51 Canadian sites (shown in Figure 9 as a scatter plot analogous to Figure 4), the ranges of vertical uplift rate swept by the expanded ensemble respect the inherent error bars in the observations. When only the

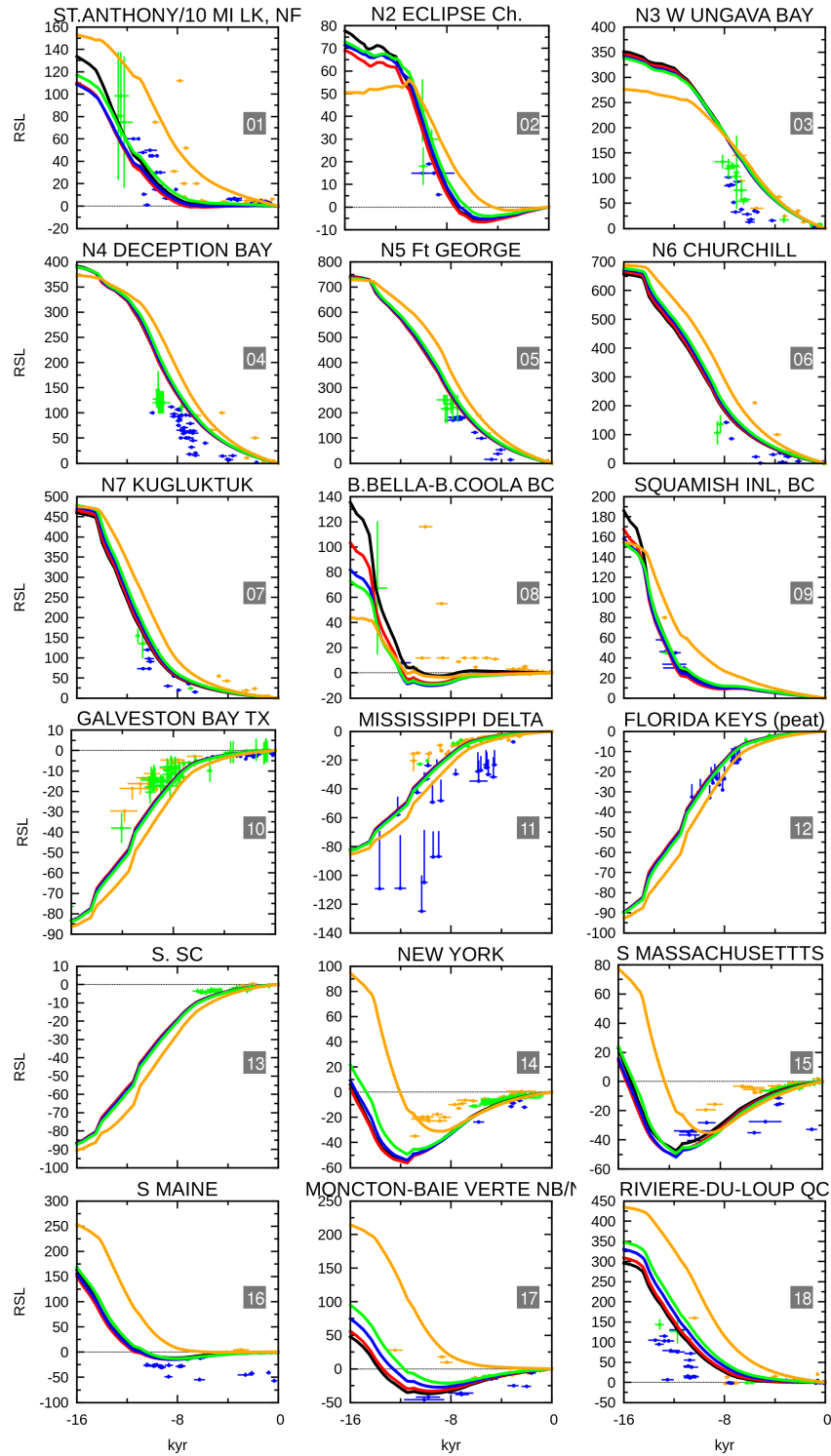


Figure 8: RSL curves from the $\tau_f = 20$ yr (red), $\tau_f = 100$ yr (blue), $\tau_f = 200$ yr (green), and $\tau_f = 1000$ yr (orange) North American simulations compared to 16G (black) and overlaid on observational data at the 18 stations discussed in Peltier et al. (2015).

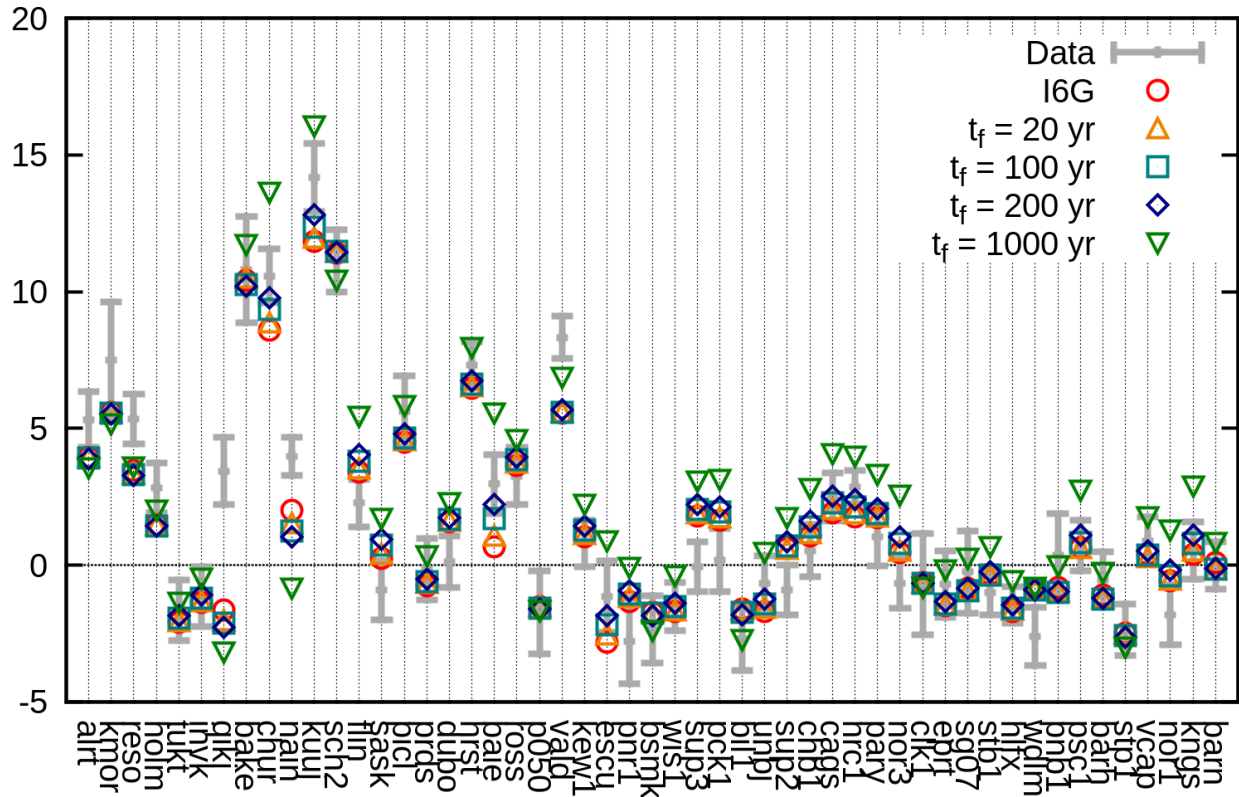


Figure 9: Scatter plot comparing simulated uplift rates from cases with $\tau_f = 20$ yr (orange triangles), $\tau_f = 100$ yr (cyan squares), $\tau_f = 200$ yr (blue diamonds), and $\tau_f = 1000$ yr (green inverted triangles) with I6G (red circles) and with observations at representative stations.

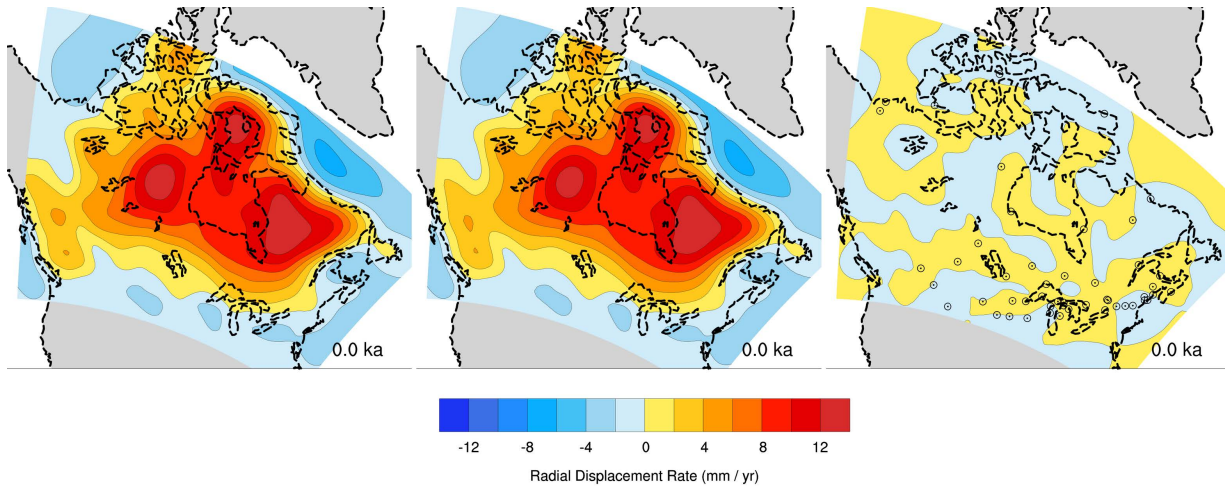


Figure 10: Modern vertical displacement rates (in mm/s) computed for Canada by applying the full GIA-SLA theory to I6G (left) and to simulation results with $\tau_f = 20$ yr (middle). The right frame shows the difference between the two, and the locations of the 51 sites at which I6G to GPS observations are compared.

three most strongly nudged ($\tau_f = 20$ yr, $\tau_f = 100$ yr, and $\tau_f = 200$ yr) simulations are considered, the ice-sheet dynamical results once again agree with I6G much better than I6G agrees with the observations. Hence, both the RSL and vertical displacement fits provide a rationale for considering the additional $\tau_f = 1000$ yr case in order to get a better idea of how the residual errors in I6G might arise from inadequate dynamical “smoothing.”

Representing the analogues of Figures 5 and 6 for Antarctica, Figures 10 and 11 show contour plots comparing the I6G prediction of modern vertical uplift distribution with results from the 4 nudged simulations (indicating the 51 sites referenced by the scatter plot in Figure 9). From Figure 10, it can be shown that there is no discrepancy between I6G and the simulation nudged at $\tau_f = 20$ yr. Figure 11 shows deviations of significant amplitude appearing only for the $\tau_f = 1000$ yr simulation in the rightmost frame. Unlike in the Antarctic results depicted in Figures 5 and 6, the geographical distribution of dynamically sensitive regions cannot be straightforwardly associated with still-existing ice-sheet features like margins and coastal grounding lines. Over the paleoclimate history of Canada, such structures would have undergone many reconfigurations to leave a complex signature in modern vertical displacement rate. Figure 12 presents a clearer picture of instantaneous patterns of dynamical sensitivity by showing, analogously to Figure 7, the nudging mass balance adjustment, ΔG , at 60 kyr BP for all four simulations. With regards to the $\tau_f = 1000$ yr case in the lower-right frame of Figure 12, the amplitudes of anomalous mass balances fall well within the $\mathcal{O}(1$ m/yr) limit that can be ascribed to uncertainties in surface precipitation and ablation. Noting that variations in ice-sheet thickness are bounded at $\mathcal{O}(1$ km), it

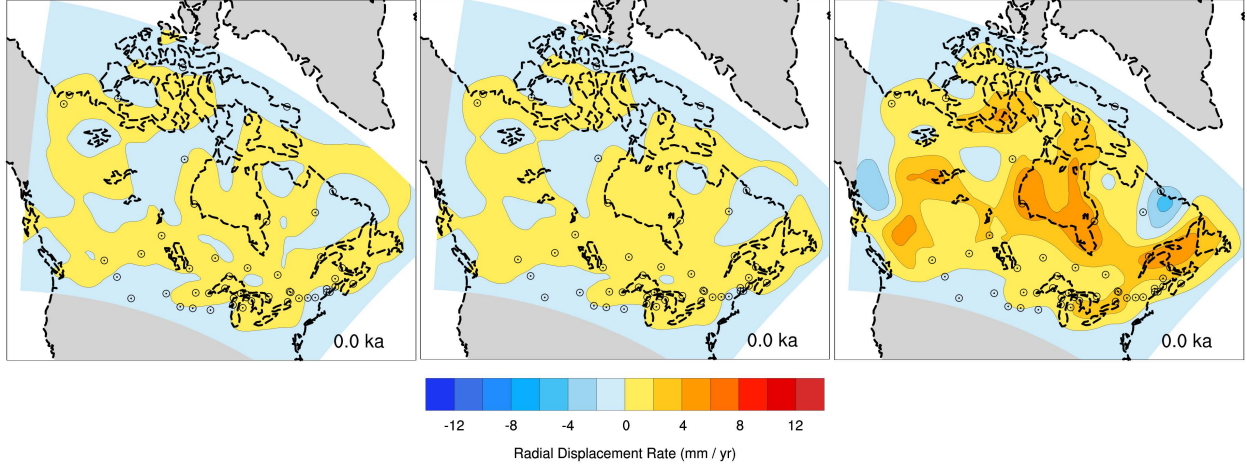


Figure 11: Modern vertical displacement rate misfits analogous to the right ($\tau_f = 20$ yr) frame in Figure 10 for $\tau_f = 100$ yr (left), $\tau_f = 200$ yr (middle), and $\tau_f = 200$ yr (right) nudging time scales.

can be anticipated on *a priori* grounds that nudging at or above this time-scale is straightforwardly rational in the paleoclimate context. The $\tau_f = 100$ yr and $\tau_f = 200$ yr cases (upper right and lower left frames) exhibit larger adjustment amplitudes, but these can, as in the corresponding Greenland and Antarctic results, be accounted for in terms of marginal and coastal structures in the ice-sheet that existed at 60 kyr BP. Such an interpretation becomes problematic only in application to the $\tau_f = 20$ yr case (upper left frame), in which the high-amplitude “noise” in the mass balance adjustment may arise (aphysically) from the “sharp edges” in the (undersmoothed) original I6G reconstruction.

Even though the $\tau_f = 20$ yr simulation exhibits signs of undersmoothing, it is logically appropriate to retain it in our ensemble for purposes of error estimation. The same considerations apply at the other end of the spectrum, where closer examination of other fields from the $\tau_f = 1000$ yr reveals signs of *undersmoothing*. While arising from a mass balance adjustment and respecting the RSL and vertical motion constraints, the solution deviates from reality by showing significant glaciation persisting to the present day. Based upon the premise that the optimally consistent solution must lie between the over- and undersmoothed extremes, the $\tau_f = 100$ yr case is selected as the Canadian “reference” solution while the entire ensemble is used to estimate local variability using a simple calculation. If $\Xi(\mathbf{x}, t; \tau_f)$ is an arbitrary field from the simulation with nudging time scale τ_f , one can estimate $\Delta\Xi(\mathbf{x}, t; 100\text{yr})$ by using linear least squares fitting over the ensemble to evaluate the local slope ($\Xi_{\tau_f}(\mathbf{x}, t; \tau)$ for $\tau = 100$ yr) of the following approximation: i.e.,

$$\Xi(\mathbf{x}, t; \tau_f) \approx \Xi(\mathbf{x}, t; \tau) + \Xi_{\tau_f}(\mathbf{x}, t; \tau)(\tau_f - \tau) \quad (12)$$

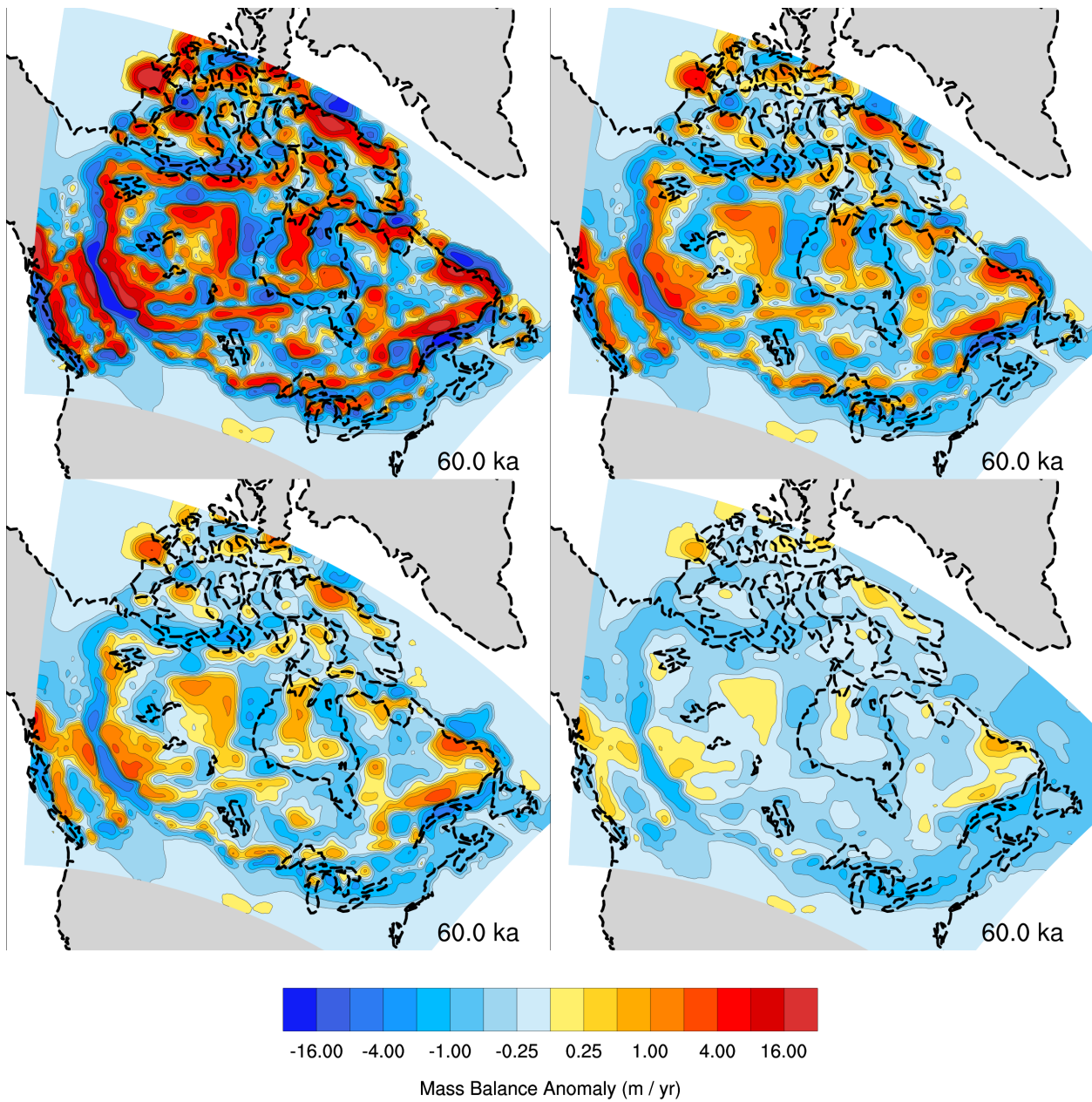


Figure 12: North American mass balances from the nudging term, ΔG in simulations with $\tau_f = 20$ yr (upper left), $\tau_f = 100$ yr (upper right), $\tau_f = 200$ yr (lower left), and $\tau_f = 1000$ yr (lower right).

and then estimating the error as

$$\Delta\Xi(\mathbf{x}, t; \tau) \approx \Xi(\mathbf{x}, t; \tau) - \Xi(\mathbf{x}, t; 0) = \tau\Xi_{\tau_f}(\mathbf{x}, t; \tau), \quad (13)$$

in which $\Xi(\mathbf{x}, t; 0)$ is the notional value of the field for a simulation that would instantaneously relax to I6G in the mass balance.

2.6 Canadian Reference Solution Fields and Variability

After validating the leading order mass balances of nudged ice-sheet dynamical simulations by the preceding methods, one can query the associated model outputs for physical information that may be of relevance to nuclear waste repository site assessments and other applications. Owing to its central role in the preceding discussions, it is natural to begin by considering the ice thickness field, l , and its associated error, Δl . The fields from the reference solution are shown in contour plots in Figure 13 for 4 times spanning the last deglaciation from LGM to present. The contours of Δl in the right frames are appropriately more closely spaced than l contours in the left frames, and are permitted to span negative values. Looking at the distributions of the thick, geographically contracting ice-sheets in the left frames, one notes that the ice model represents these sharply delimited structures surrounded by extended regions of thin ice that is some tens of meters thick. Even after glaciation has almost completely disappeared, this superficial ice cover persists over a large region of the Canadian Arctic. The “virtual” ice obviously is not a real feature of the present environment, but the model nevertheless remains consistent because its thickness falls within the magnitude of the corresponding error estimate.

Beyond simply being consistent with zero ice thickness within error, the superficial ice cover in the reference solution plays a logically beneficial role by facilitating the representation of basal phenomenology that would not be captured if the underlying regions were perfectly ice free. Where ice exists, permafrost thickness may, for instance, be diagnosed from a lithospheric thermal buffer layer that couples the lower thermodynamic BC of Eqs. 7 to geothermal heat fluxes. Permafrost is known to be thickest just in those regions with little or no surface ice because the basal frictional heating action of thick, moving ice sheets tends to thaw frozen ground. Figures 14 and 15 highlight this effect in respective contour plots of permafrost thickness and basal temperature from the reference solution (along, once again, with corresponding error estimates). There are clear, sharp boundaries separating glaciated areas with relatively warm basal temperatures and relatively thin permafrost layers from periglacial areas with cold basal temperatures and thick permafrost. This phenomenology would not be captured if the ice-sheet model did not impose a superficial ice cover over the latter regions. Insofar as the virtual ice shown in Figure 13 covers the modern Canadian Arctic, it corresponds quite well with the measured extent of year-round permafrost. From what little is known about the detailed distribution of permafrost depth, the modern configuration depicted

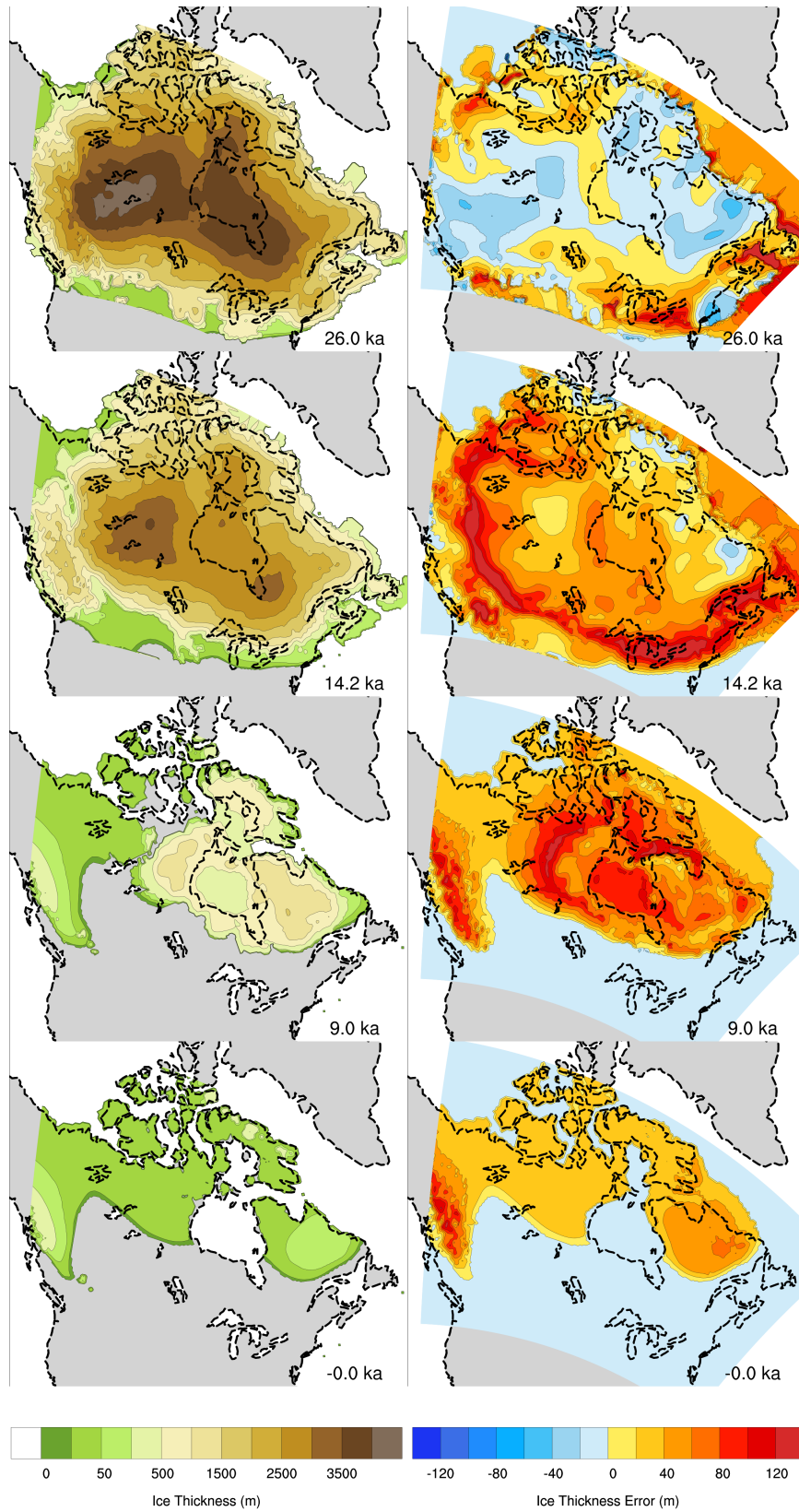


Figure 13: Reference solution ice thickness, I (left), and error, ΔI (right), at $t = 26$ kyr BP (LGM), 14.2 kyr BP, 9 kyr BP, and present.

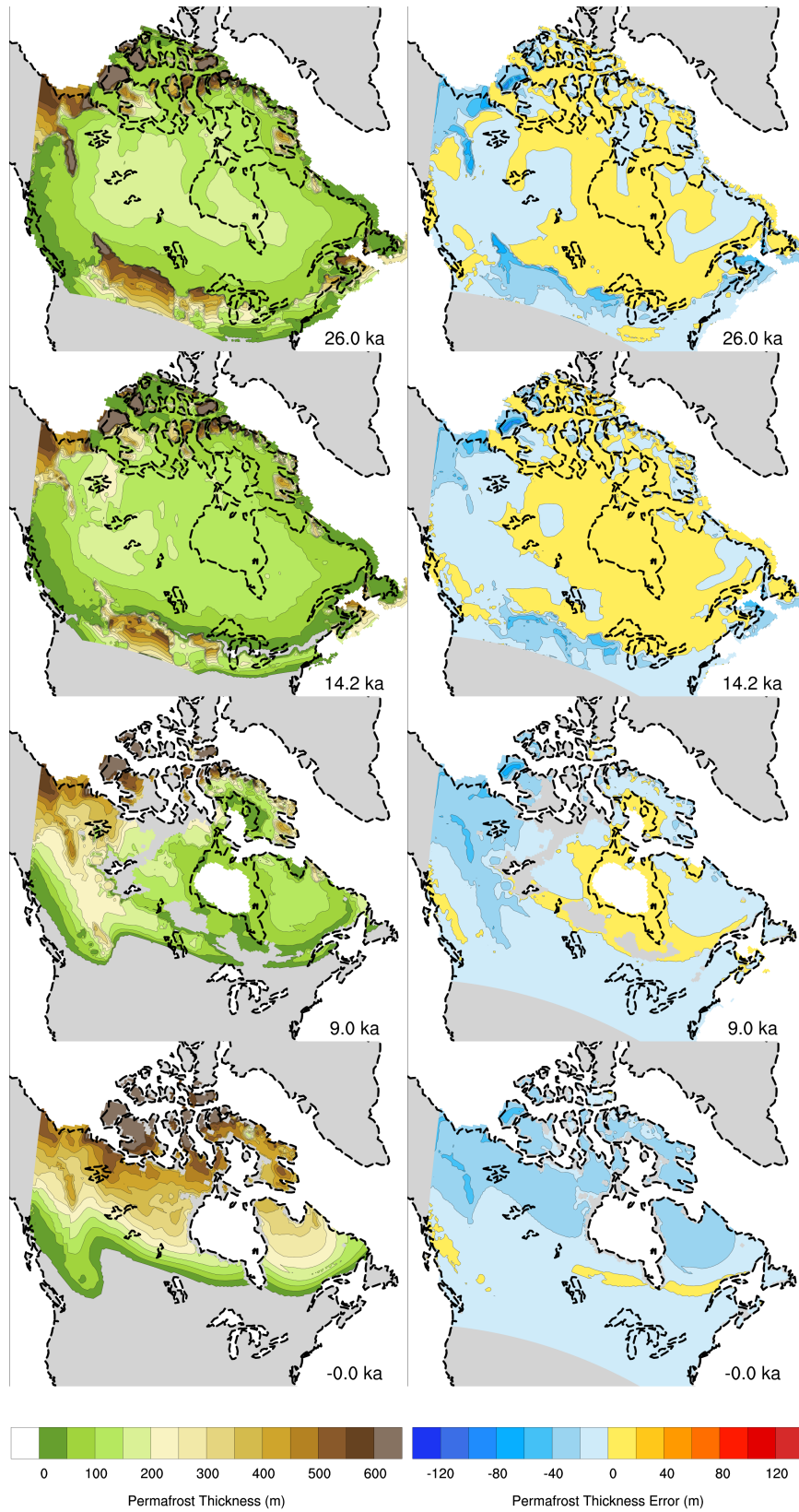


Figure 14: Permafrost thickness and corresponding error from the solution referenced in Figure 13.

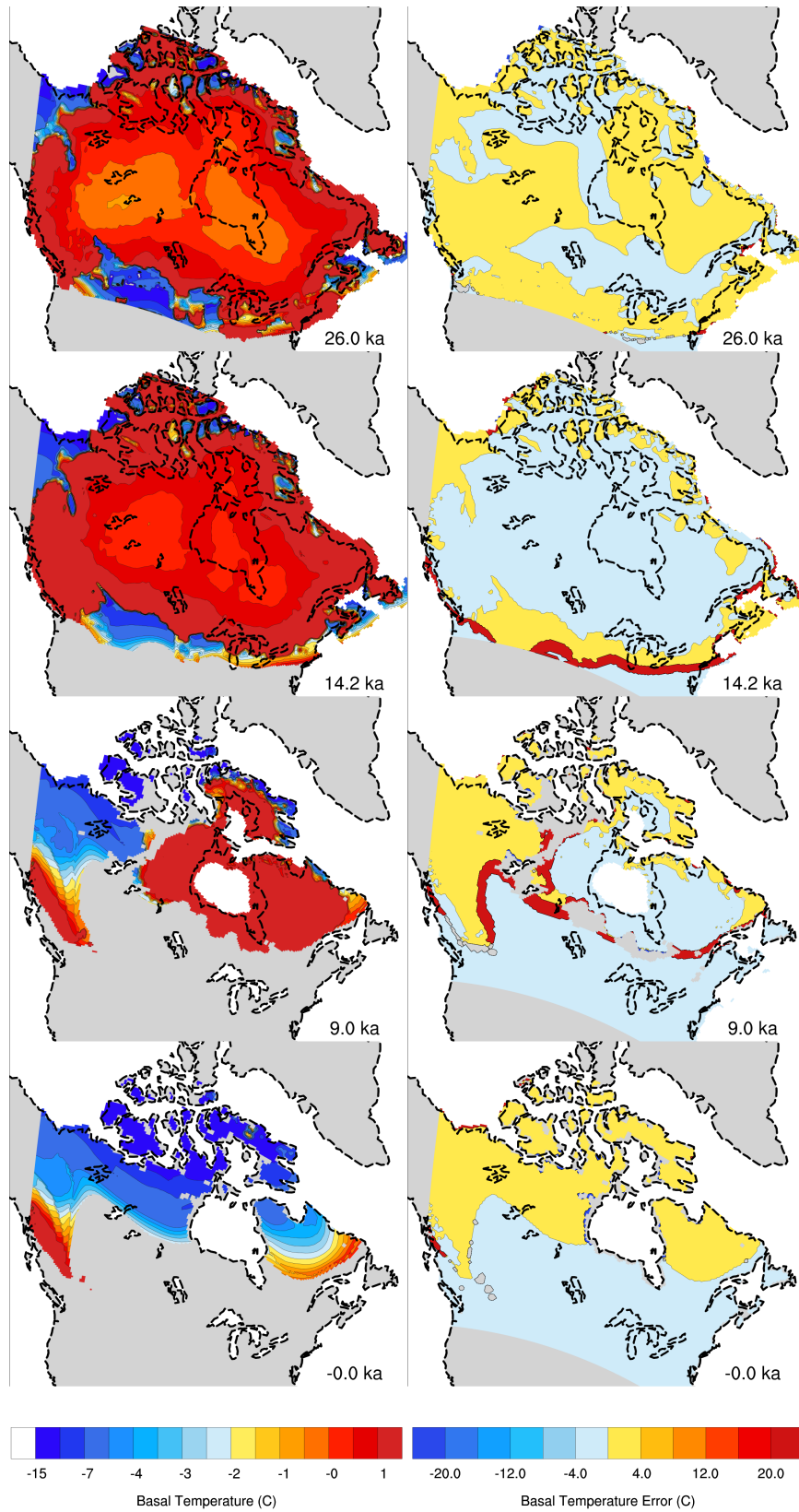


Figure 15: Basal temperature and corresponding error from the solution referenced in Figure 13.

in Figure 14 is reasonable.

In regions where thick ice-sheets are present, there is a close dynamical coupling between heating due to friction, meltwater production, basal sliding, and basal shear stress. The new PISM-based UofTGSM framework represents these physics in much more detailed fashion than the version from which the results discussed by Peltier (2006) originated. Complete with corresponding error estimates, Figure 16 shows contour plots of basal meltwater production while Figures 17, 18 show vector plots of basal velocity and shear stress, respectively. Meltwater production and basal sliding appear to be localized in a way that suggests ice “streaming” in plausible locations, while the shear stress vector field shows much less sign of localization. Based upon our error estimation procedure, the shear stress also appears to be more robustly represented than velocity, which shows signs of large variability in some regions of rapid sliding (note the relative scaling between solution and error vector scales in Figure 18).

2.7 Lake Depth

The fields considered in the previous subsection are all accessible as intrinsic elements of ice-sheet dynamical simulations, which naturally supply all but one of the paleoclimate surface BCs that NWMO requested for site studies. To achieve logically rigorous predictions of surface lake depth (the outstanding surface BC), the dynamics of the model would have to be coupled to a proper dynamical representation of surface watersheds and groundwater. Even though the new PISM-based UofTGSM framework represents temperate ice with included meltwater and carries a rudimentary groundwater budget coupled to its basal sliding parameterization, it cannot inherently predict surface lake depth. Earlier UofTGSM versions used heuristics to diagnose lake depth predictions that were needed to drive linear groundwater models (McKenzie et al., 2007; Lemieux et al., 2008a,b), but these techniques were never well validated and cannot be straightforwardly transferred into the new framework.

However, another heuristic may be devised based upon premises that are easy to explain in the new logical framework. A discrete depression-fill algorithm by effective nonlinear diffusion can be expressed in terms of the following steps:

1. Define an ice/solid-surface topography, $B_* \equiv B + I$, and smooth it over the numerical mesh using a simple Laplacian kernel.
2. Define an initial, gravitationally inconsistent water level, W_0 , everywhere on the surface as

$$W_0 = B_* + t_M M + t_G \begin{cases} -G & \text{if } G < 0 \\ 0 & \text{otherwise,} \end{cases}$$

which amounts to sitting a “bolus” consisting of t_M years’ worth of meltwater and t_G years’ worth of negative mass balance (typically ice loss) on top of the smoothed topography.

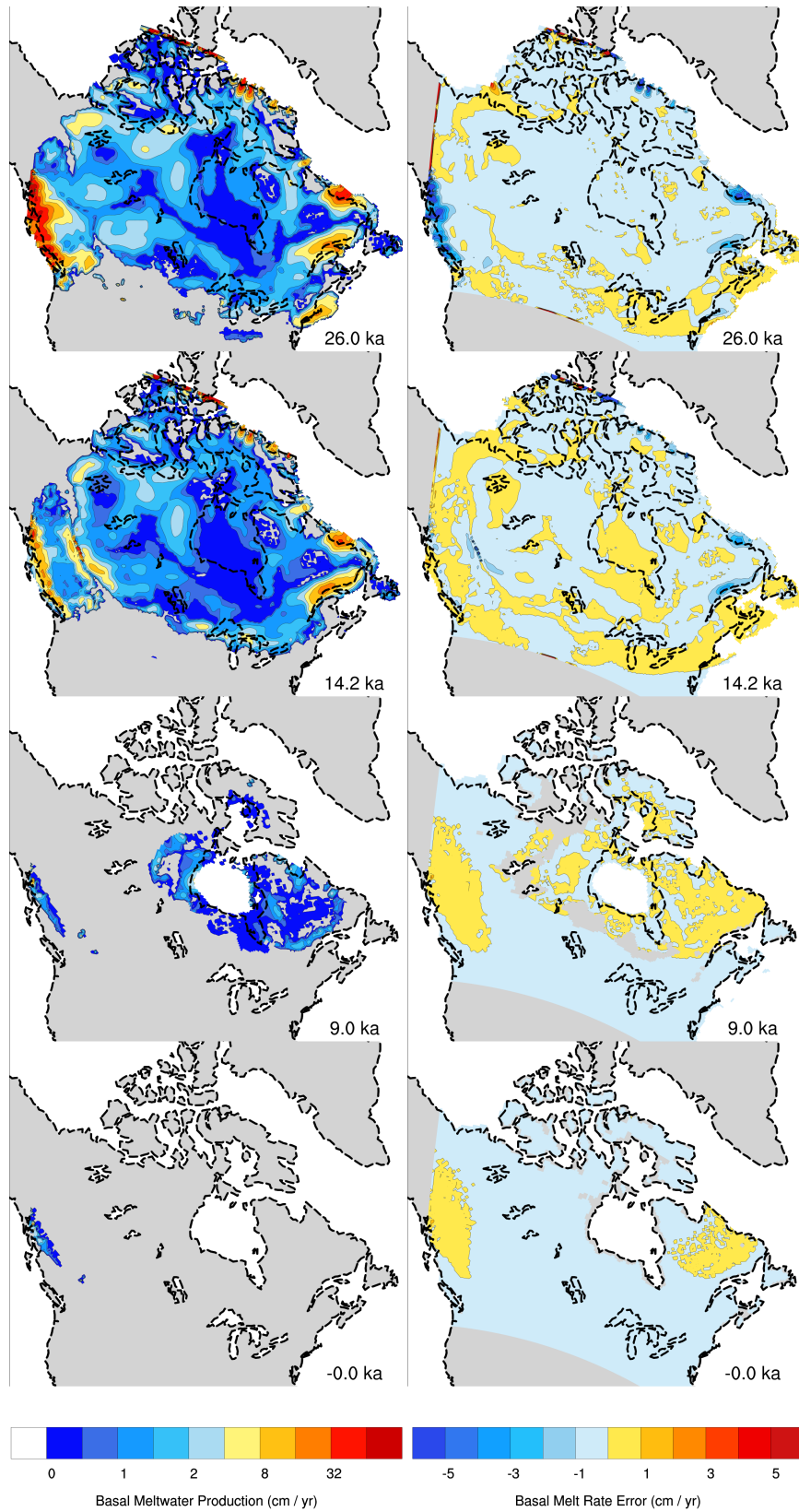


Figure 16: Basal meltwater production and corresponding error from the solution referenced in Figure 13.

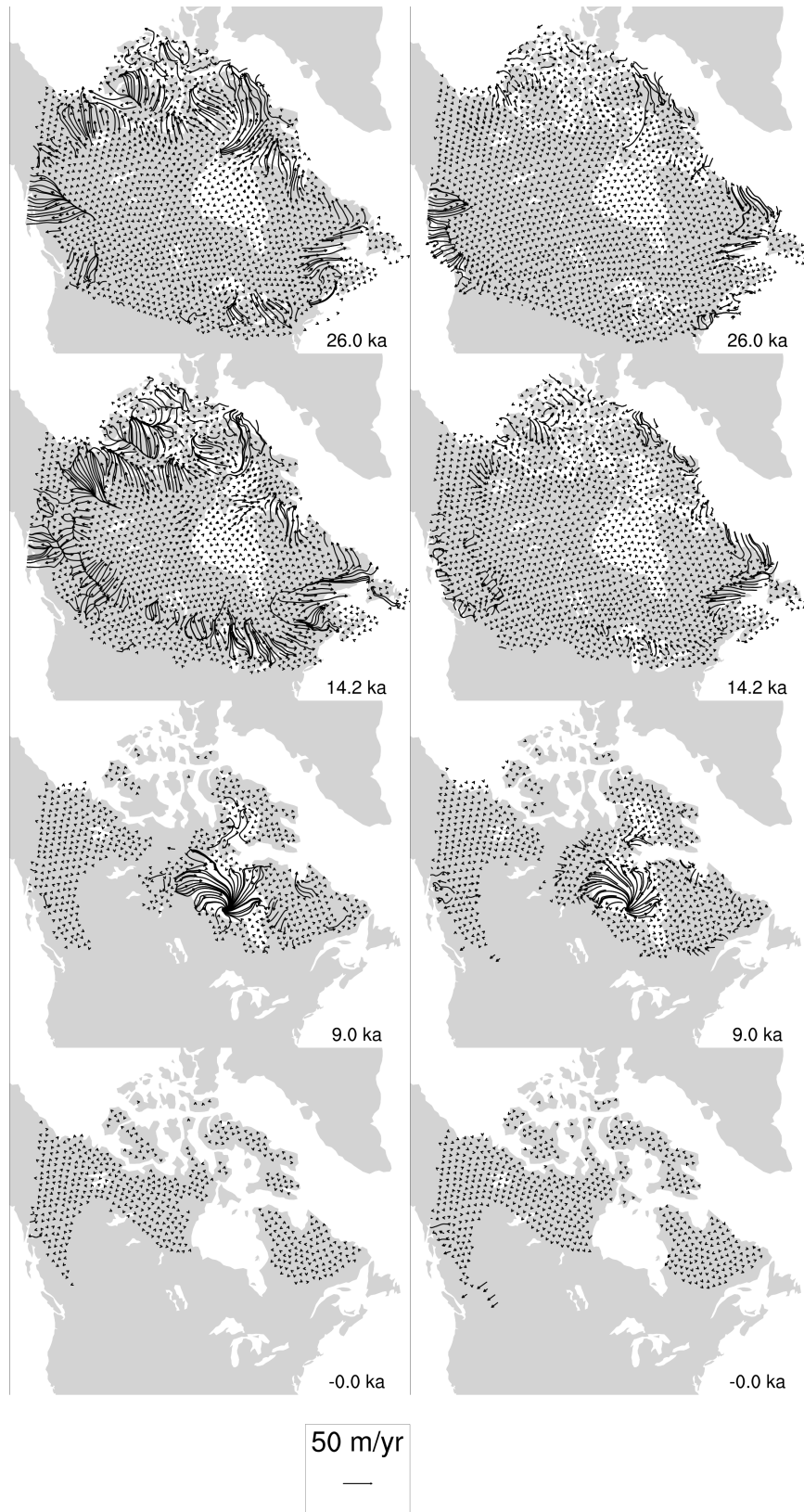


Figure 17: Basal velocity and corresponding error from the solution referenced in Figure 13.

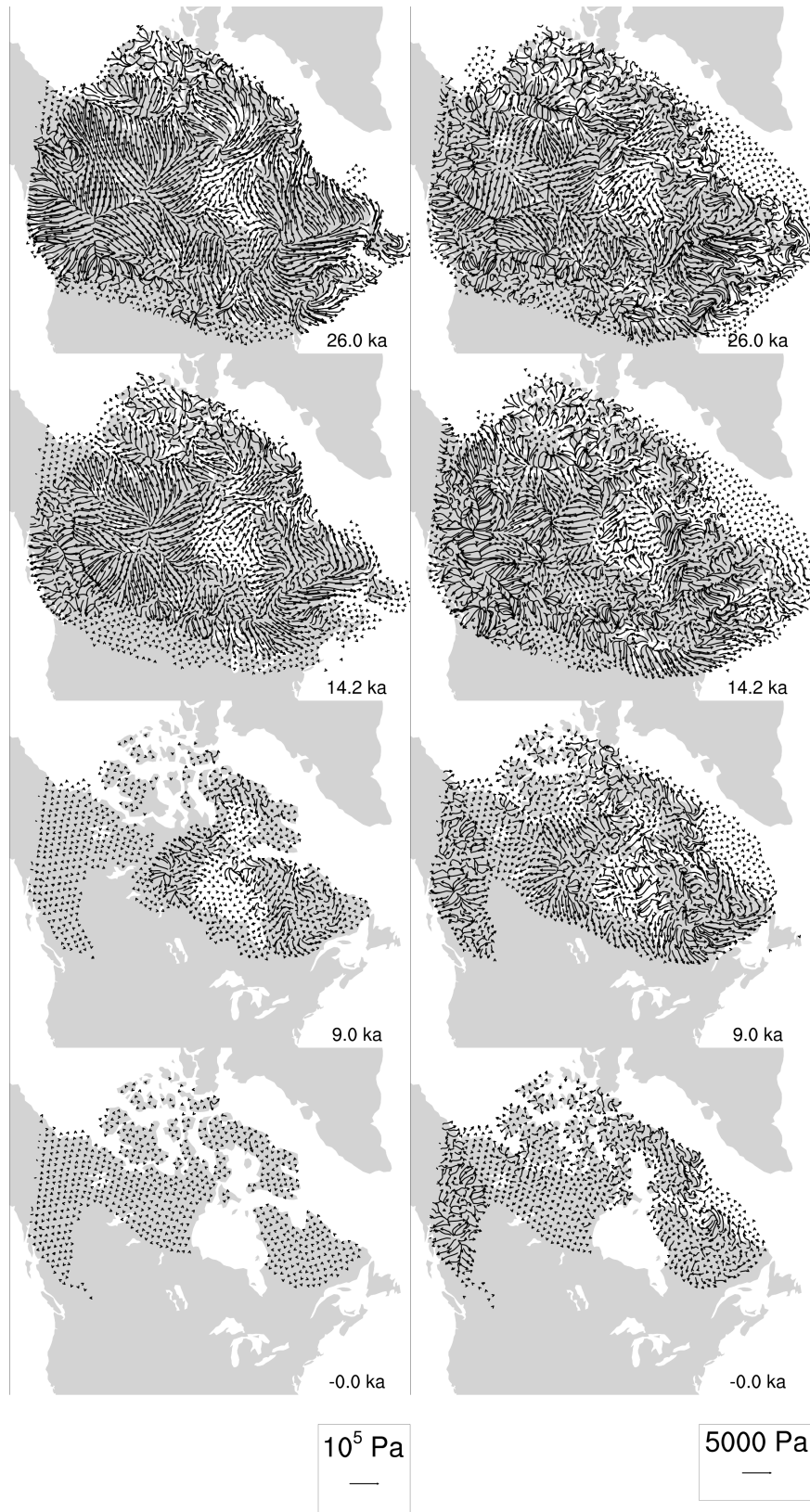


Figure 18: Vertical basal shear stress and corresponding error from the solution referenced in Figure 13.

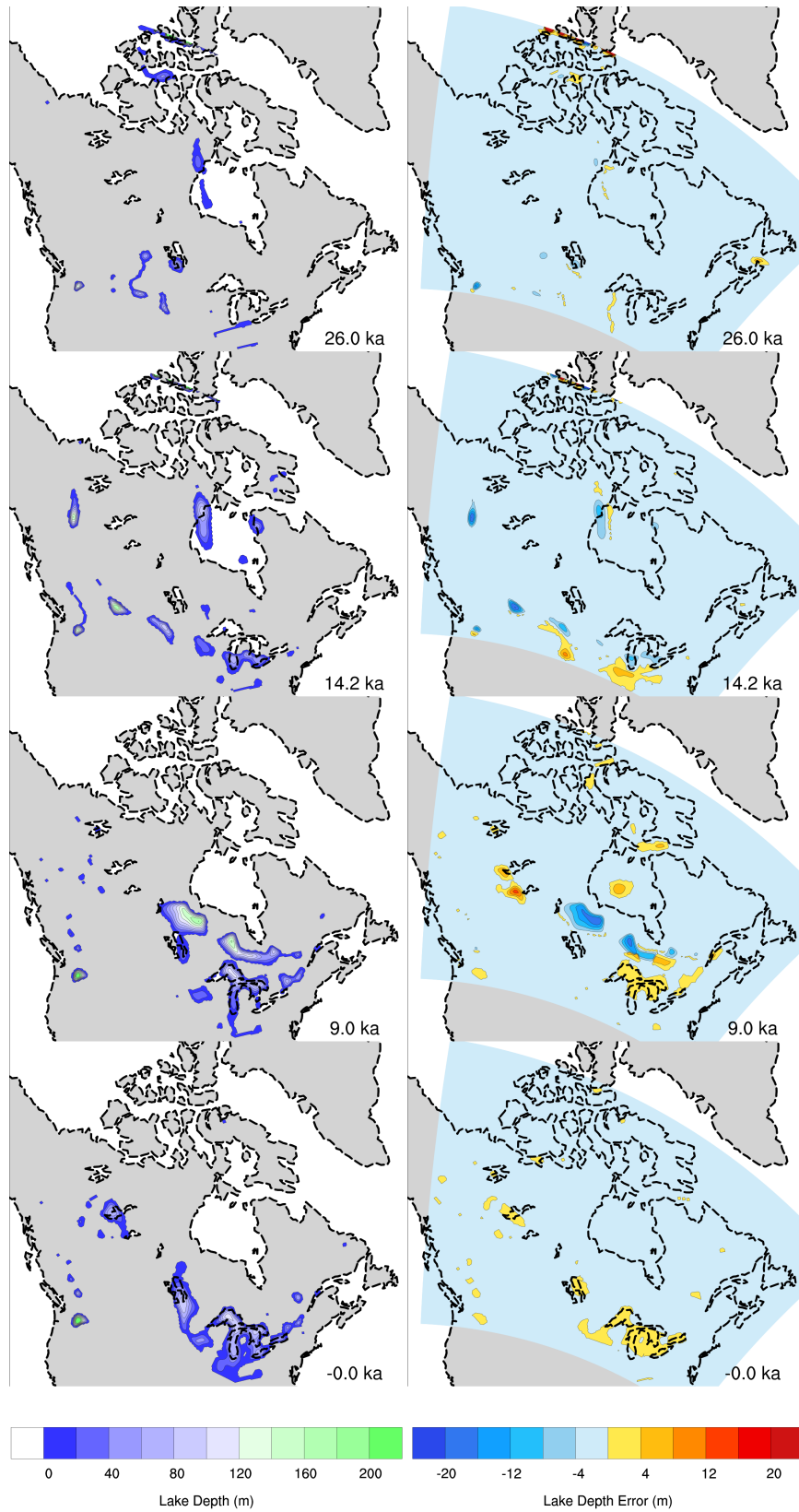


Figure 19: Lake depth and corresponding error from the solution referenced in Figure 13.

3. Simulate the gravitational adjustment of W_0 by repeatedly iterating through steps 4 through 8 to determine W_i from W_{i-1} .
4. Visiting each edge in the grid in sequence, compare the average water level of the two adjacent cells to the topographic height of each cell.
5. If it is greater than both, then set both water levels to the average.
6. If the average water level falls below the bottom of one cell, transfer all of the water in that cell to the other (steps 4 through 6 locally conserve mass if grid cells are all the same size).
7. After all of the grid edges have been visited for the current iteration, set the water level to zero at the boundary edges (presuming that there is drainage into a deep recession outside the domain).
8. Where water level has fallen below 0 (i.e., below sea level), set it to 0 on the presumption that this cell is covered by ocean, and not by lakes.

This methodology is simplified, but Figure 19 shows that it can diagnose reasonably credible forecasts of lake occurrences and depths from instantaneous “snapshots” of the ice-dynamical solution. 200 iterations is generally sufficient to converge to a stable depression fill pattern. t_G was tuned to 3 yr to give reasonable modern Great Lake depths, albeit with some overflow in smoothed topography falling close to the domain boundary. Occurrences and depths of proglacial lakes can be tuned more closely by the t_M parameter, for which a 100 yr value produces the illustrated results with credible 9 kyr BP positions and depths for Lakes Agassiz and Ojibway. The error prediction for the modern solution is not sufficient to encompass the discrepancies, but the results are acceptable.

3. DISCUSSION

Figures 20 through 22 show composite contour plots of grounded ice elevation, floating ice thickness, and lake depth at the same 36 time-levels that Peltier (2006) used for similar plots. The netCDF file accompanying this report includes all fields saved as two-dimensional geographic distributions at the 147 time-levels used by the I6G model. The data is mapped to a polar stereographic grid with x and y spacings of about 25 km, and the projection parameters are documented as attributes of the “mapping” variable. Time series may be extracted at the location of any potential Canadian repository site, and Figures 23 and 24 show local comparisons of some results with corresponding results from Peltier (2006) at the previously studied 4CS site and from Peltier (2011) at the previously studied 5CS site. Figure 24 includes additional comparisons of bedrock

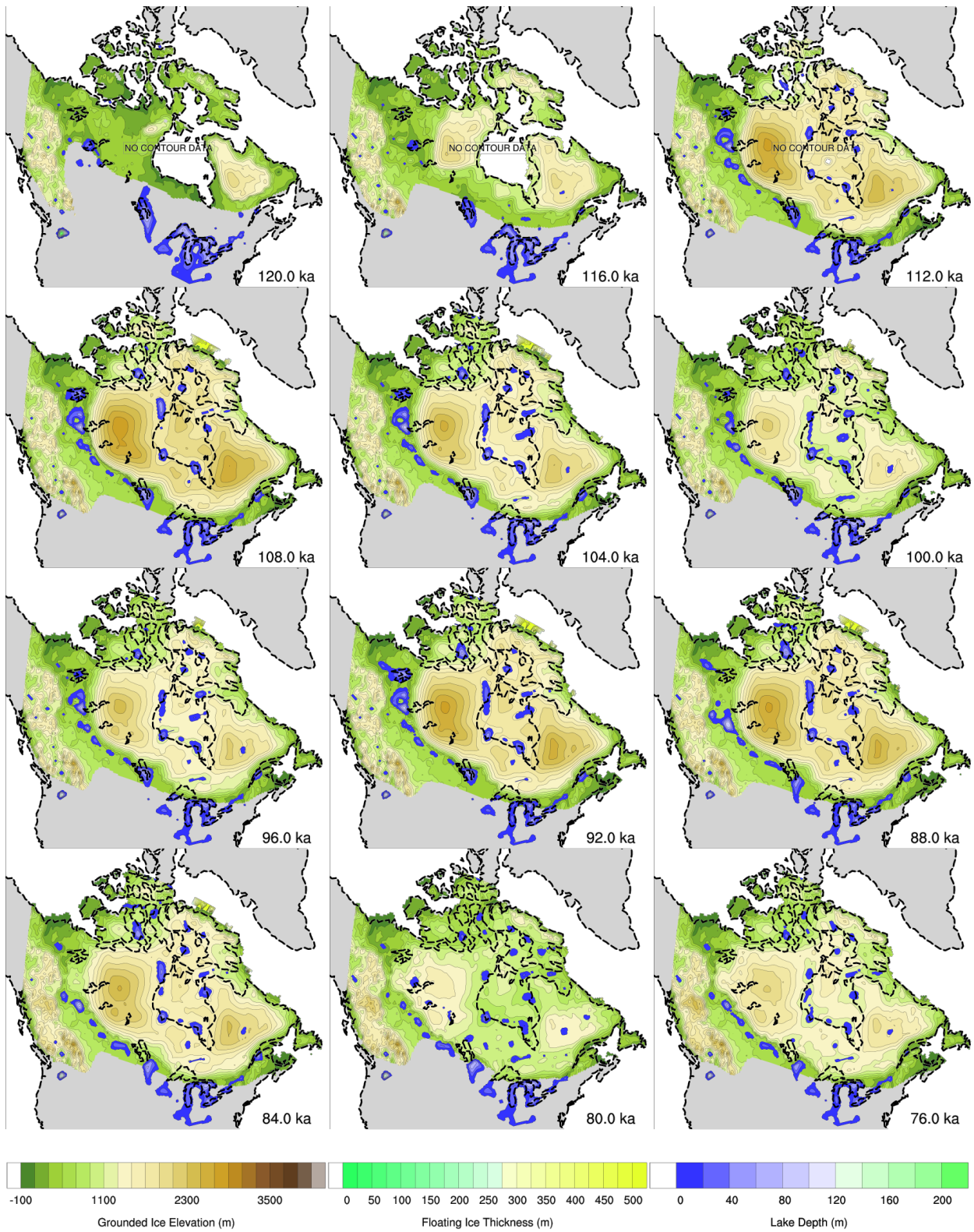


Figure 20: Composite contour plots of grounded ice elevation, floating ice thickness, and lake depth at times considered in Peltier (2006)

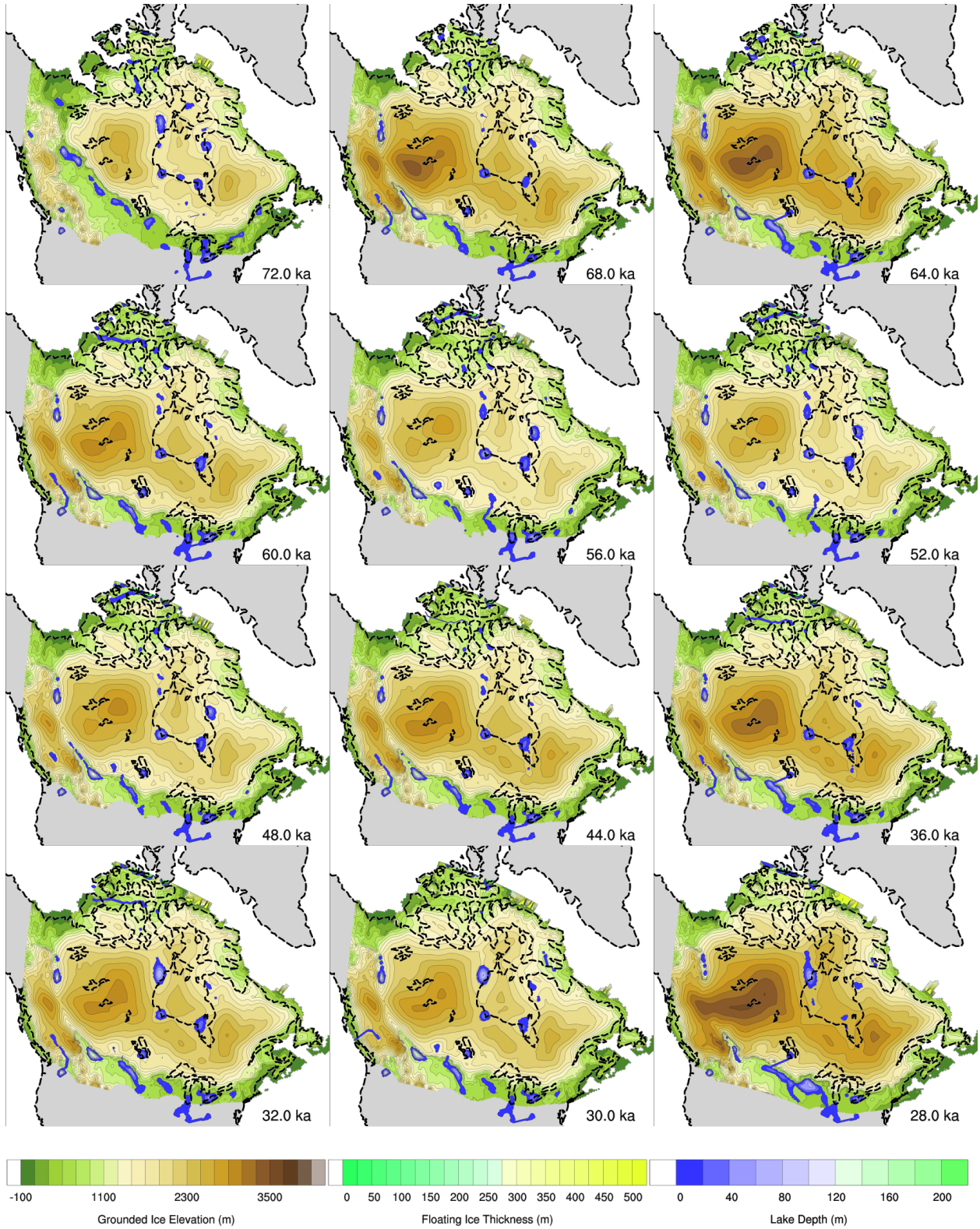


Figure 21: Continuation of Figure 20.

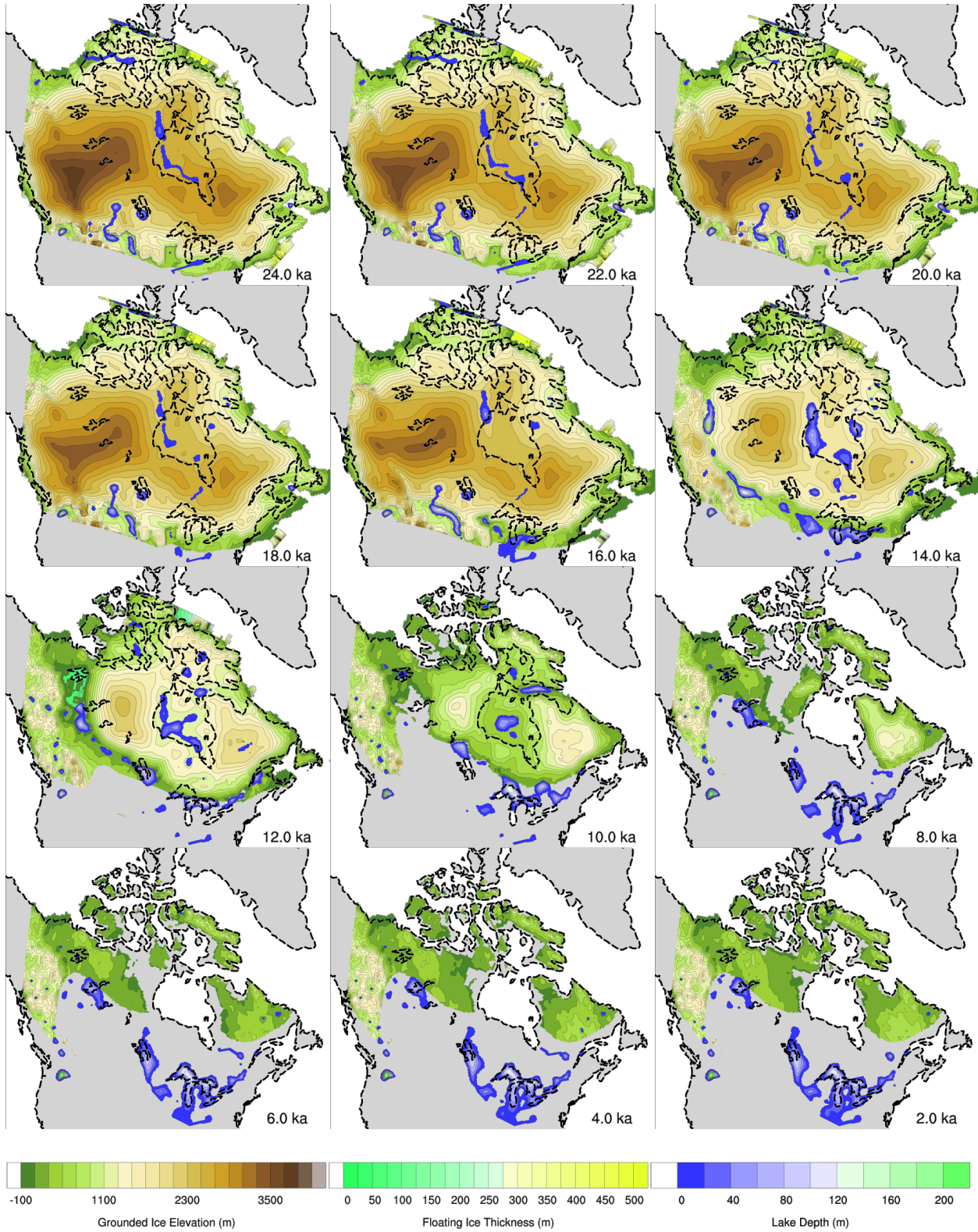


Figure 22: Continuation of Figures 20 and 21.

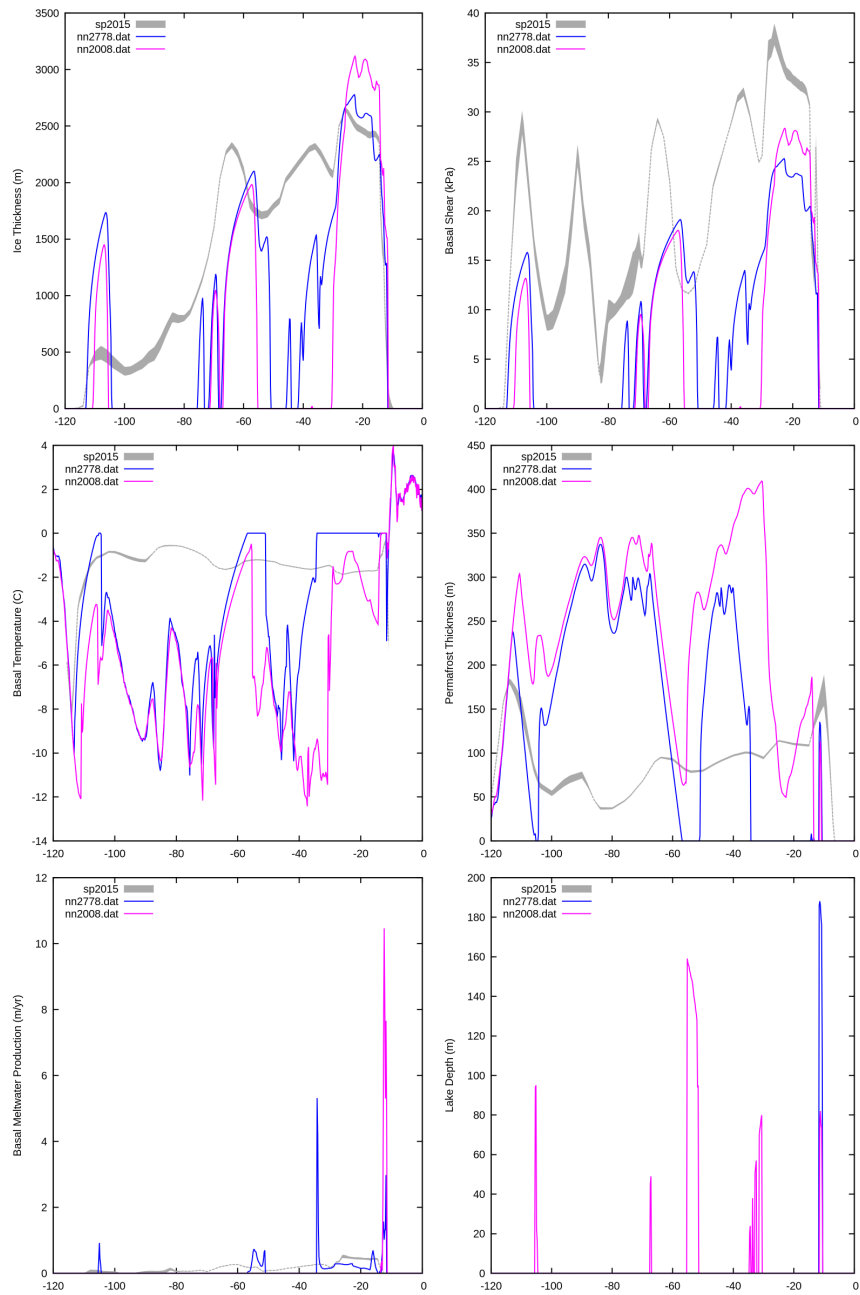


Figure 23: Time series of selected fields at the 4CS site, shown with error margins and compared with the nn2008 and nn2778 cases of Peltier (2006).

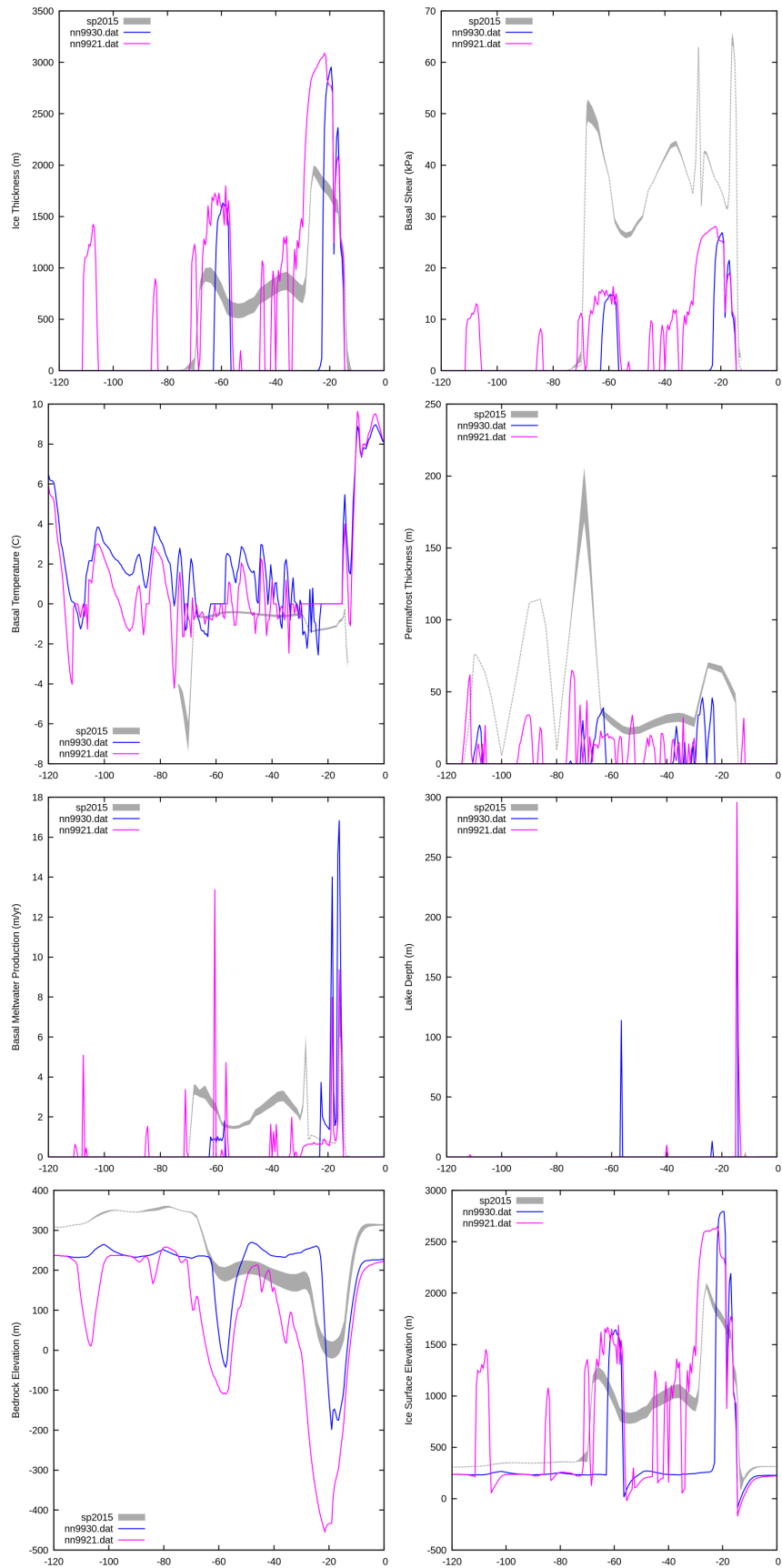


Figure 24: Time series of selected fields at the 5CS site, shown with error margins and compared with the nn9921 and nn9930 cases of Peltier (2011).

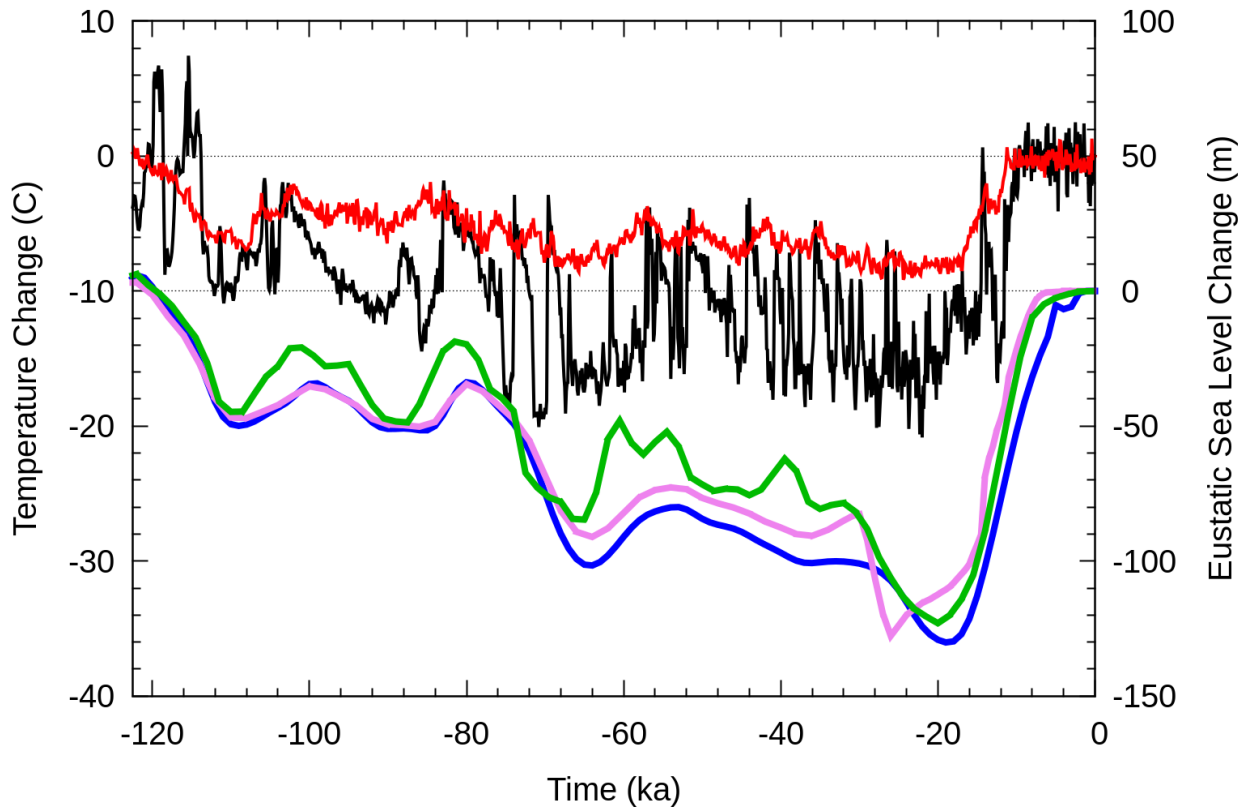


Figure 25: Time series of climatological temperature adjustment, $\Delta T(t)$, inferred from the Greenland GRIP ice core (black) and the Antarctic Vostok ice core (red). The SPECMAP time series of eustatic sea-level change is shown (in blue) along with a version corrected for ocean temperature (green) and an estimate based on eustatic sea-level equivalent I6G ice volume change (in violet). The y-scale for sea levels is shown on the right axis.

surface and ice surface elevations that derive from the ice surface through the GIA solution procedure. The error information in the new results (labelled sp2015) is used to plot shaded ranges that are indicative of the time evolution of local dynamical variability. Figures 23 and 24 show that solutions exhibit signals that have comparable amplitudes and that correlate well with each other in time, although the amplitudes of differences between solutions (including differences between the nn_{xxxx} solutions in an ensemble) are comparable to the amplitudes of the solutions themselves. There is a clear overlap between the time intervals over which the nn_{xxxx} solutions exhibit strong intermittency and the time intervals over which the new nudged solution ensemble predicts the greatest dynamical variability (especially in the ice thickness and normal stress fields). Considering the previously mentioned difficulty of estimating lake depth and the improvements that have been made to the representation of physics at the base of the ice-sheet, variations in the detailed characteristics of the corresponding time-series are understandable. For purposes of the present discussion, the most notable difference between the Peltier (2006, 2011) solutions and the latest UofTGSM results is in the fact that the former predict a rapid, intermittent sequence of glaciations and deglaciations at the 4CS and 5CS sites while the latter predict a “smoother” progression of increases and decreases in land-ice thickness over the last 100kyr glacial cycle.

The relatively “smoother” temporal evolution seen in the new sp2015 solutions may be understood in relation to the plots in Figure 25, which compares ice core-based inferences of surface temperature variation with records of eustatic sea-level variation. $\Delta T(t)$ estimates are from the GRIP ice core site in Greenland (Johnsen et al., 1997, in black) and from the Vostok ice core site in Antarctica (Petit et al., 2001, in red), while eustatic sea-level estimates are from the SPECMAP data set (Imbrie and McIntyre, 2006, in blue), from an alternative version corrected for variations in ocean temperature (Waelbroeck et al., 2002, in green), and from the eustatic component of the I6G reconstruction (in violet). Since the freezing and melting of the Canadian ice-sheets represents the dominant contribution to global sea-level change over the last glacial cycle, the absence of strong intermittency in all of the eustatic sea-level records contradicts the sporadic ice cover predicted by the simulations of Peltier (2006, 2011). By nudging the new simulations towards I6G, we limit the extent to which ice-sheet dynamics are influenced by the much higher frequency temporal variability that is evident in ice core-based temperature inferences. Since it is inherently questionable to make assumptions about temperature variation across North America based upon an isolated ice core record from Greenland, the “smoothness” of the new results is very likely to be more realistic than the intermittency seen in previous results. Intermittent glaciation prior to LGM remains a statistical possibility because observational constraints apply mostly to deglaciation since LGM, but the absence of “smoothly” glaciated cases from the nn_{xxxx} ensembles was a shortcoming that has now been addressed.

The base methodology was justified in detail in the main section of this Report and in other literature, and the remaining discussion clarifies how the newly established framework constitutes

a sound bases for further exploration and development of the dataset. The preceding comparisons of time-series at the 4CS and 5CS sites show how nudging supplies a much more practical basis for estimates of error and uncertainty than the application of Bayesian calibration to model parameters. The new ice-sheet modelling framework consistently agrees with observations on the assumption of widely used and reasonable parameter choices, but does not invalidate the earlier approach behind the datasets of Peltier (2006). When simulation ensembles automatically suppress inconsistent solutions of the kind that are bound to arise with random parameter sweeps, it becomes more straightforward to apply any technique that analyzes the effects of parameters beyond the nudging time scale τ_f upon the detailed qualities of results in the main Report section. Additional parameter studies are a natural avenue for further research, and it is, moreover, evident from results discussed herein, in SP, and elsewhere that I6G itself supplies an imperfect and non-unique fit to the ever expanding array of observations constraining historical glaciation. Such analyzes may shed light upon the even greater uncertainties that limit model-based predictions of potential future glaciation in the context of natural and anthropogenic climate change. Discounting the long-term effects of greenhouse gas emissions and considering astronomically determined orbital insolation characteristics, Peltier (2011) estimated that a re-glaciation of the Canadian land mass would be possible approximately 60 kyr from now. Subsequent extensions of this analysis have revealed a second, more likely expansion of land-ice cover beginning around 125 kyr in the future. Further work is needed to ascertain how these scenarios would be affected by other, less predictable climate variations.

4. SUMMARY AND CONCLUSIONS

By nudging to the observationally consistent I6G ice-thickness history, an advanced ice-sheet model has been tuned to provide empirically consistent paleoclimate dynamical BCs and associated error estimates. The methodology has been validated with respect to the still-existing Greenland and Antarctic ice-sheets, and then applied to the generation of a dataset describing Canadian ice-sheets over the last 100 kyr glacial cycle. While remaining consistent in the leading-order sense with the methodology and results of Peltier (2006), the new work incorporates improvements that can be broadly summarized in terms of the following points:

- The version of the UofTGSM used to produce the new dataset reflects the current state-of-the-art in physical understanding and numerical technology, and includes many advances over Peltier (2006) (e.g., coupling SIA-based ice-sheet dynamics to an SSA-based ice-shelf approximation; improving representations of calving and glacial-till related processes; using enthalpy-based thermodynamics to represent ice-water mixtures at melting point; etc.).
- The observations that have gone into tuning the I6G ice-sheet thickness histories (and there-

fore, indirectly, the nudged simulations) include many new measurements that did not exist at the time Peltier (2006) was submitted (e.g., GPS and satellite measurements and exposure-age dating results).

- Without contradicting the logic supporting Bayesian parameter selection, the nudging procedure provides a more practical and empirically workable framework for local error estimation. Bayesian techniques will be of use in more refined explorations of observationally-constrained model parameter spaces.
- The new dataset fully represents model-derived physical quantities as time-varying distributions over the North-American continent.

REFERENCES

- Argus, D. F., W. R. Peltier, R. Drummond, and S. Moore (2014), The antarctic component of glacial isostatic adjustment model ICE-6G_C (VM5a) based upon GPS measurements of vertical motion of the crust, exposure age dating of ice thickness variations and relative sea level histories, *Geophys J. Int.*, 198, 537–563.
- Bindschadler, R. A., S. Nowicki, A. Abe-Ouchi, A. Aschwanden, H. Choi, J. Fastook, G. Granzow, R. Greve, G. Gutowski, U. Herzfeld, et al. (2013), Ice-sheet model sensitivities to environmental forcing and their use in projecting future sea level (the SeaRISE project), *Journal of Glaciology*, 59(214), 195–224.
- Clark, J. A., W. E. Farrell, and W. R. Peltier (1978), Global changes in postglacial sea level: a numerical calculation, *Quaternary Research*, 9(3), 265–287.
- Farrell, W., and J. A. Clark (1976), On postglacial sea level, *Geophysical Journal International*, 46(3), 647–667.
- Imbrie, J., and A. McIntyre (2006), SPECMAP time scale developed by Imbrie et al., 1984 based on normalized planktonic records (normalized O-18 vs. time, specmap. 017), *Earth Syst Sci Data*, 10.
- Johnsen, S. J., H. B. Clausen, W. Dansgaard, N. S. Gundestrup, C. U. Hammer, U. Andersen, K. K. Andersen, C. S. Hvidberg, D. Dahl-Jensen, J. P. Steffensen, et al. (1997), The $\delta^{18}\text{O}$ record along the Greenland Ice Core Project deep ice core and the problem of possible Eemian climatic instability, *Journal of Geophysical Research: Oceans* (1978–2012), 102(C12), 26,397–26,410.
- Joughin, I., B. E. Smith, and B. Medley (2014), Marine ice sheet collapse potentially under way for the thwaites glacier basin, west antarctica, *Science*, 344(6185), 735–738.
- Lemieux, J., E. Sudicky, W. Peltier, and L. Tarasov (2008a), Dynamics of groundwater recharge and seepage over the canadian landscape during the wisconsinian glaciation, *Journal of Geophysical Research*, 113(1), 1–18.
- Lemieux, J., E. Sudicky, W. Peltier, and L. Tarasov (2008b), Simulating the impact of glaciations on continental groundwater flow systems: 1. relevant processes and model formulation, *Journal of Geophysical Research*, 113(F3), F03,017.
- Marshall, S. J., L. Tarasov, G. K. Clarke, and W. R. Peltier (2000), Glaciological reconstruction of the laurentide ice sheet: physical processes and modelling challenges, *Canadian Journal of Earth Sciences*, 37(5), 769–793.

- McKenzie, J., C. Voss, and D. Siegel (2007), Groundwater flow with energy transport and water–ice phase change: Numerical simulations, benchmarks, and application to freezing in peat bogs, *Advances in water resources*, 30(4), 966–983.
- Nowicki, S., R. A. Bindschadler, A. Abe-Ouchi, A. Aschwanden, E. Bueller, H. Choi, J. Fastook, G. Granzow, R. Greve, G. Gutowski, et al. (2013a), Insights into spatial sensitivities of ice mass response to environmental change from the SeaRISE ice sheet modeling project I: Antarctica, *Journal of Geophysical Research: Earth Surface*, 118(2), 1002–1024.
- Nowicki, S., R. A. Bindschadler, A. Abe-Ouchi, A. Aschwanden, E. Bueller, H. Choi, J. Fastook, G. Granzow, R. Greve, G. Gutowski, et al. (2013b), Insights into spatial sensitivities of ice mass response to environmental change from the SeaRISE ice sheet modeling project II: Greenland, *Journal of Geophysical Research: Earth Surface*, 118(2), 1025–1044.
- Pattyn, F., L. Perichon, A. Aschwanden, B. Breuer, B. De Smedt, O. Gagliardini, G. H. Gudmundsson, R. Hindmarsh, A. Hubbard, J. V. Johnson, et al. (2008), Benchmark experiments for higher-order and full Stokes ice sheet models (ISMIP-HOM), *The Cryosphere Discussions*, 2(1), 111–151.
- Peltier, W. (1974), The impulse response of a Maxwell Earth, *Reviews of Geophysics*, 12(4), 649–669.
- Peltier, W. (1976a), Glacial-Isostatic Adjustment-II. The Inverse Problem, *Geophysical Journal of the Royal astronomical society*, 46(3), 669–705.
- Peltier, W. (1976b), Glacio-isostatic adjustment-III. The inverse problem, *Geophysics Journal*, 46, 669–706.
- Peltier, W. (1998), Postglacial variations in the level of the sea: Implications for climate dynamics and solid-earth geophysics, *Reviews of Geophysics*, 36(4), 603–689.
- Peltier, W. (2007), *History of Earth rotation*, vol. 9, pp. 243–293, Elsevier Oxford.
- Peltier, W., and J. Andrews (1976), Glacial-Isostatic AdjustmentI. The Forward Problem, *Geophysical Journal of the Royal Astronomical Society*, 46(3), 605–646.
- Peltier, W., and S. B. Luthcke (2009), On the origins of Earth rotation anomalies: New insights on the basis of both “paleogeodetic” data and Gravity Recovery and Climate Experiment (GRACE) data, *Journal of Geophysical Research: Solid Earth (1978–2012)*, 114(B11).
- Peltier, W., W. Farrell, and J. Clark (1978), Glacial isostasy and relative sea level: a global finite element model, *Tectonophysics*, 50(2), 81–110.

- Peltier, W., R. Drummond, and K. Roy (2012), Comment on "Ocean mass from GRACE and glacial isostatic adjustment by DP Chambers et al., *Journal of Geophysical Research: Solid Earth* (1978–2012), 117(B11).
- Peltier, W. R. (2006), Boundary conditions data sets for spent fuel repository performance assessment, Tech. Rep. 06819-REP-01200-10154-R00, Ontario Power Generation, Inc., Toronto, Ontario.
- Peltier, W. R. (2011), Long-term climate change, Tech. Rep. NWMO DGR-TR-2011-14, Nuclear Waste Management Organization, Toronto, Ontario.
- Peltier, W. R., D. F. Argus, and R. Drummond (2015), Space geodesy constrains ice age terminal deglaciation: The global ICE-6G_C (VM5a) model, *Journal of Geophysical Research: Solid Earth*, 119, 1–38.
- Petit, J., D. Jouzel, D. Raynaud, N. Barkov, J. Barnola, I. Basile, M. Bender, J. Chappellaz, J. Davis, G. Delaygue, et al. (2001), Vostok Ice Core Data for 420,000 Years, IGBP PAGES/World Data Center for Paleoclimatology Data Contribution Series# 2001-076, NOAA/NGDC Paleoclimatology Program, Boulder CO, USA.
- Pollard, D., and R. M. DeConto (2009), Modelling west antarctic ice sheet growth and collapse through the past five million years, *Nature*, 458(7236), 329–332.
- Ritz, C., A. Fabre, and A. Letréguilly (1996), Sensitivity of a greenland ice sheet model to ice flow and ablation parameters: consequences for the evolution through the last climatic cycle, *Climate Dynamics*, 13(1), 11–23.
- Salameh, T., P. Drobinski, and T. Dubos (2010), The effect of indiscriminate nudging time on large and small scales in regional climate modelling: application to the mediterranean basin, *Quarterly Journal of the Royal Meteorological Society*, 136(646), 170–182.
- Stuhne, G., and W. Peltier (2015), Reconciling the ICE-6G_C reconstruction of glacial chronology with ice sheet dynamics: the cases of Greenland and Antarctica, *Journal of Geophysical Research: Land Surface*, 120, 1841–1865.
- Tarasov, L., and W. Peltier (1997), Terminating the 100 kyr ice age cycle, *Journal of Geophysical Research*, 102(D18), 21,665–21.
- Tarasov, L., and W. Peltier (1999), Impact of thermomechanical ice sheet coupling on a model of the 100 kyr ice age cycle, *Journal of Geophysical Research. D. Atmospheres*, 104, 9517–9545.
- Tarasov, L., and W. Peltier (2000), Laurentide ice sheet aspect ratio in models based on glen's flow law, *Annals of Glaciology*, 30(1), 177–186.

- Tarasov, L., and W. Peltier (2002), Greenland glacial history and local geodynamic consequences, *Geophys. J. Int.*, 150, 198–229.
- Tarasov, L., and W. Peltier (2003), Greenland glacial history, borehole constraints, and eemian extent, *J. Geophys. Res.*, 108(2143), 10–1029.
- Tarasov, L., and W. Peltier (2004), A geophysically constrained large ensemble analysis of the deglacial history of the north american ice-sheet complex, *Quaternary Science Reviews*, 23(3), 359–388.
- Waelbroeck, C., L. Labeyrie, E. Michel, J. C. Duplessy, J. McManus, K. Lambeck, E. Balbon, and M. Labracherie (2002), Sea-level and deep water temperature changes derived from benthic foraminifera isotopic records, *Quaternary Science Reviews*, 21(1), 295–305.
- Winkelmann, R., M. Martin, M. Haseloff, T. Albrecht, E. Bueler, C. Khroulev, and A. Levermann (2011), The Potsdam parallel ice sheet model (PISM-PIK)—Part 1: Model description, *The Cryosphere*, 5(3), 715–726.
- Wu, P., and W. Peltier (1984), Pleistocene deglaciation and the Earth's rotation: a new analysis, *Geophysical Journal of the Royal Astronomical Society*, 76(3), 753–791.

APPENDIX A: CD ARCHIVE OF TIME SERIES

The CD that accompanies this report includes the time-varying distribution of model-derived physical quantities described in Section 2.6.